Dynamics of Atmospheres and Oceans 80 (2017) 75–96

Contents lists available at ScienceDirect

Dynamics of Atmospheres and Oceans

journal homepage: www.elsevier.com/locate/dynatmoce

A nested pre-operational model for the Egyptian shelf zone: Model configuration and validation/calibration

H. Nagy[a,*], A. Elgindy[a], N. Pinardi[b,c], M. Zavatarelli[b], P. Oddo[d]

[a] Oceanography Department, Faculty of Science University of Alexandria, Egypt
[b] Department of Physics and Astronomy, Alma Mater Studiorum University of Bologna, Bologna, Italy
[c] Centro EuroMediterraneo sui Cambiamenti Climatici, Bologna, Italy
[d] CMRE, Centre for Maritime Research and Experimentation, La Spezia, Italy

ARTICLE INFO

Article history:
Received 7 April 2017
Received in revised form 6 August 2017
Accepted 15 October 2017
Available online 16 October 2017

Keywords:
Egyptian shelf model
Nile river
Argo floats
SST data
Mesoscale features

ABSTRACT

We explored the variability of the Egyptian shelf zone circulation connected to atmospheric forcing by means of a numerical simulation of the general circulation. A high resolution model grid was used at 1/60° horizontal resolution and 25 sigma layers. The simulation was carried out using the most recent version of the Princeton Ocean Model (POM). The initialised model was run the whole year of 2006 using the analysis forcing data for the same year obtained from ECMWF and MFS (Mediterranean Forecasting System, Pinardi et al., 2003). The model skills were evaluated by means of the root mean square error (RMSE) and correlations. The Egyptian Shelf Model (EGYSHM) simulation suggests the presence of an Egyptian Shelf Slope Current (ESSC), which is flowing eastward at different depths in the domain. We found that the maximum velocity of the ESSC [0.25 m/s] is located near the continental slope during the summer time, while in winter the velocity of ESSC is weaker [0.12 m/s] in the same location. The ESSC appears to be directly affected by Mersa-Matruh gyre system. EGYSHM reproduced the main region circulation patterns, especially after adding the Nile River outflow. We found that wind stress is crucial to force the circulation of the Egyptian shelf zone. EGYSHM SST was significantly correlated to satellite SST in all months at a 95% confidence limit, with a maximum of 0.9743 which was obtained in May 2006. The RMSE between EGYSHM and Argo floats salinity data was about 0.09. We compared our results with satellite altimetry to verify the positions and shapes of mesoscale features.

1. Introduction

The Egyptian shelf zone is one of the widest continental shelves in the Levantine Basin, and was built by the accumulation of sediments from the Nile River (Frihy et al., 2003; Pinardi et al., 2005). The Egyptian zone extends from 30.75° to 33.25° N and from 25.5° to 35.5° E. In this area, the shelf is limited by a 200 m bathymetric line. However, the maximum depth of the studied zone is about 3000 m in front of the town of Mersa-Matruh, in the western part of the Egyptian coast (Fig. 1).

The coastal area of the shelf is characterised by the fresh water source of the Nile River delta mouths. The Nile has two main branches, Rosetta in the west and Damietta in the east (Fig. 1). Before the High Dam was built in 1964, the annual

---

* Corresponding author.
E-mail address: hznagy@ims.metu.edu.tr (H. Nagy).

https://doi.org/10.1016/j.dynatmoce.2017.10.003
0377-0265/

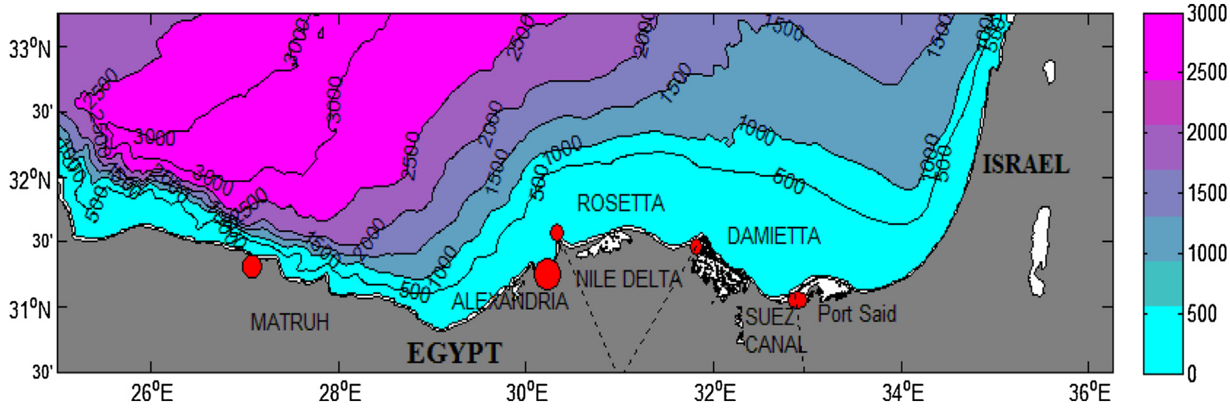

Fig. 1. The Egyptian Shelf Zone domain and bathymetry with the main Egyptian geographical sites.

discharge from both the Rosetta and Damietta was approximately 3500 $m^3 s^{-1}$. The following year, the annual discharge of the two branches was reduced to 1500 $m^3 s^{-1}$ (Halim, 1960; Halim et al., 1967; Vörösmarty et al., 1999; Nixon, 2003). This volume discharge then became even less according to Hamza et al. (2003) and Ludwig et al. (2009) reported that the flow rate now reached about 1/3 of the previously mentioned discharge rate which was 1500 $m^3 s^{-1}$.

The geostrophic currents with 400 m as a reference level in the south-eastern sector of the Mediterranean Sea were studied by Sharaf El-Din and Karam (1976) in the winter season in front of the Nile delta. The Nile low salinity plume current magnitudes were approximately 50 cm s^{-1} before building the High Dam in 1964. The other currents of the area were generally parallel to the coast and between 12 cm/s and 20 cm/s. After the High Dam was built in 1965 currents exceeded 30 cm/s. According to El-Gindy and Sharaf El-Din (1985) the deep water mass characteristics (temperature, salinity and density) off the Egyptian shelf are a mixture of Adriatic deep waters, transitional Levantine Intermediate Waters (LIW, Hecht et al., 1988) and Cretan waters (Theocharis et al., 1993). The spatial distribution of the deep-water characteristics indicated a cyclonic gyre in deep areas of the Levantine basin.

The horizontal circulation patterns of the Eastern Mediterranean Sea were calculated by Said (1990), during the winter and the summer seasons. The geostrophic current was calculated using 1000 m as a reference level. Said (1990) found that the geostrophic current velocities varied between 5 and 30 cm/s off the Libyan coasts, 15–25 cm/s near the Egyptian coasts and 35–40 cm/s in the eastern part of the Levantine Sea. The POEM program (Robinson et al., 1992) detected for the first time from hydrographic data a large anticyclone structure on the western side of the Egyptian shelf, so-called Mersa-Matruh anticyclonic gyre, partly distorting the eastward currents along the shore. A few years earlier, the deep area of the Eastern Levantine basin had also been found to be dominated by mesoscales (Robinson et al., 1991) and anticyclonic gyres of a recurrent nature (Hecht et al., 1988).

In the Egyptian shelf waters, two main water masses dominate. The Modified Atlantic Water (MAW), which characteristics are seasonally variable due to air sea interactions (El-Gindy, 1984) with a range for temperatures equal to 14–19 °C and salinities equal to 37.7–38.4 PSU (POEM Group, 1992; Malanotte-Rizzoli et al., 1997; Nittis and Lascaratos, 1998). The MAW is generally found between 30–80 m depth. Below this layer the salinity increases with depth to a maximum at the core of Levantine Intermediate Water (LIW) at about 150–400 m depth. Sharaf El-Din and El-Gindy (1986) studied the proportion of the water types contributing to LIW and concluded that they were formed by Atlantic water from the Sicilian straits, deep waters from the Adriatic Sea and the Levantine intermediate water type formed in winter. The LIW overall ranges for temperature, salinity and σ_θ according to POEM Group (1992) are 14–15 °C, 38.8–38.9 PSU and 29.00–29.17 kg m^{-3} respectively. The region below 500 m is occupied by deep waters of the Eastern Mediterranean which is nearly homogenous. The range of temperatures, salinities and σ_θ are 13–13.7 °C, 38.6–38.7 PSU and 29.17–29.19 kg m^{-3} respectively (El-Gindy, 1984; Malanotte-Rizzoli et al., 1997).

Said and Rajkovic (1996) studied the water circulation with a 22 km resolution model along the Egyptian coasts. They found that the Mersa-Matruh anticyclone gyre exhibited a strong winter-to-summer variability, moving from anticyclonic to cyclonic. Said and Rajkovic (1996) discovered an anticyclonic gyre in the southeastern part of the Levantine Sea. They called this pattern the “El-Arish gyre”, which was present during spring and autumn, while it disappeared during summer. In order to study the water circulation and the hydrographic structure of the southeastern Levantine, Alam El-Din et al. (2000) applied a numerical model with a resolution of approximately 12 km. The model showed that the eastward flow parallel to the coast was the main feature of the general circulation along the Egyptian coast.

Since 1999 the Mediterranean Forecasting System (MFS) has been producing daily forecasts and analyses for the entire Mediterranean Sea (Pinardi et al., 2003; Pinardi and Coppini, 2010). Furthermore MFS produces re-analyses for the entire Mediterranean Sea (Adani et al., 2011) that offer the opportunity to study the climatological circulation of the basin. Pinardi et al. (2015) described the south-eastern Levantine surface circulation as dominated by the Southern Levantine Current (SLC) which shows a decadal variability associated with the Northern Ionian reversal phenomenon.

Korres and Lascaratos (2003) implemented a one-way nested eddy-resolving model of the Aegean and Levantine basins (ALERMO). Implementation started with resolution of 1/20° × 1/20° and was recently upgraded to 1/50° × 1/50°. The authors showed that the ALERMO model nested to the MFS could successfully reproduce the coarse model solution and at the same time modify this solution adding finer resolution structures. Sofianos et al. (2006) found that the differences in the domain mean kinetic energy between the "slave" and the "active" ALERMO model simulations were significant in both September 2004 and January 2005 experiments, with the "active" experiments being much more energetic.

Zodiatis et al. (2001, 2006) used a numerical model to study the circulation of the north-eastern part of the Levantine basin. They used the Cyprus Coastal Model (CYCOM) nested with the Aegean-Levantine Regional Model (ALERMO). The results showed that the Mid-Mediterranean jet separated into two branches – one going southwest of Cyprus and the other eastwards. The southwest jet created the eastern extension of the Rhodes cyclonic gyre located to the west of Cyprus and the eastward current flows up to the Lattakia basin, joining the Asia Minor Current.

Ibrahim (2003) used a numerical model with a resolution of approximately 3.5 km with 14 vertical sigma layers. Again, the Egyptian shelf circulation was found to be dominated by the westerly flow along the coast. In the western region of the shelf, the Mersa Matruh anticyclone gyre was present, occupying the area between 27°E to 28°E longitudes. A cyclonic gyre between 28°E and 30°E longitudes was also found and the El-Arish anticyclone gyre appeared at the eastern side of the Egyptian shelf together with a weak anti-cyclonic gyre in front of the Nile Delta.

Brenner et al. (2006) assessed one-year high-resolution operational forecasts for the southeastern Mediterranean shelf region. Both the MFS and the southeastern Mediterranean shelf model underestimated the high salinity of the Levantine Surface Water (LSW), which is presumably linked to the crude specification of the surface freshwater flux in both models at that time (i.e., a relaxation to surface salinity climatology). They also noted that the strong drop in surface salinity in the climatological curve was associated with the freshwater input from the Nile flood, which reached its annual maximum in September during the pre-Aswan High Dam period, prior to 1965. They found that most of the errors in their model results were due to the initial conditions.

This study explores, for what we believe is the first time, the variability of the Egyptian shelf zone circulation connected to a specific year, 2006, and by means of a high resolution numerical model. This is the basic calibration/validation study in order to start operational forecasting in the Egyptian shelf zone. We show the implementation of an Egyptian shelf zone (EGYSHM) model with a horizontal resolution of 1/60° × 1/60° and 25 vertical sigma levels. The basin scale MFS model is at 1/16° × 1/16° resolution and is described in Tonani et al. (2008) giving daily average lateral boundary conditions to EGYSHM. Monthly climatological Nile River discharges were obtained from Vörösmarty et al. (1999). The model is also provided with surface water flux boundary conditions. EGYSHM was used in the "active" mode, where it was initialized only once from MFS. The model is compared with satellite SST data, Argo temperature and salinity profiles in March 2006 and satellite sea level anomalies.

Section 2 describes the model implementation, and the nesting procedures. Section 3 reports the simulation results during 2006. Section 4 presents validation results and Section 5 provides the discussion and conclusions.

2. Model design and implementation

The numerical simulations were carried out using the latest version of Princeton Ocean Model (POM, Blumberg and Mellor, 1987), which is a 3D finite difference, free surface numerical model, utilizing the Boussinesq and the hydrostatic approximations with a time split mode algorithm for the internal and external modes. All the equations are written in rectangular coordinates and contain spatially and temporally varying horizontal eddy viscosity and diffusion coefficients. The model solves the following equations for the ocean velocity ($\vec{u}$) = (u, v, w), potential temperature (T) and salinity (S):

$$\vec{\nabla}.\vec{u} = 0 \tag{1}$$

$$\frac{\partial(u,v)}{\partial t} + \vec{u}.\nabla(u,v) + f(-v,u) = -\frac{1}{\rho_0}\left(\frac{\partial p}{\partial x}, \frac{\partial p}{\partial y}\right) + \nabla_h.[A_M\nabla(u,v)] + \frac{\partial}{\partial z}\left[K_M\frac{\partial(u,v)}{\partial z}\right] \tag{2}$$

$$\frac{\partial p}{\partial z} = -\rho(x,y,z,t)\,g \tag{3}$$

$$\frac{\partial T}{\partial t} + \vec{u}\cdot\nabla T = \nabla_h\cdot(A_M\nabla_h T) + \frac{\partial}{\partial z}(K_H\frac{\partial T}{\partial z}) + \frac{1}{\rho_0 C_p}\frac{\partial I}{\partial z} \tag{4}$$

$$\frac{\partial S}{\partial t} + \vec{u}\cdot\nabla S = \nabla_h\cdot(A_M\nabla_h S) + \frac{\partial}{\partial z}(K_H\frac{\partial S}{\partial z}) \tag{5}$$

where ρ is the sea water density in (kg m^{-3}) calculated by an adapted UNESCO equation of state devised by Mellor (1991). The eddy horizontal viscosity A_M coefficient (m^2 s^{-1}) is provided by the Smagorinsky (1993) parameterization implemented in POM following Mellor and Blumberg (1985). The vertical mixing coefficients for momentum (K_M) and tracers (K_H) in (m^2 s^{-1}) are calculated using the Mellor and Yamada (1982) turbulence closure scheme. The last term in Eq. (4) is the parameterization

Table 1
The Nile Delta climatological monthly averaged discharge for a 12-year period (1975–1986) in m^3/s according to Vörösmarty et al. (1999) and Nixon (2003).

Month	Total Nile Delta discharge in m^3/s
January	1239.4
February	1034.4
March	1126.1
April	1111.1
May	1170.3
June	1540.2
July	1740.8
August	1556.1
September	1190.3
October	1103.9
November	1076.2
December	1154.8

of the heat penetration in the water column as indicated by Pinardi et al. (2003) and where ρ_o is the reference density in ($kg\,m^{-3}$), and C_p is the specific heat for the sea water. The approximation for the penetrative short wave radiation is provided by Jerlov (1976) according to:

$$I(z) = Q_S Tr\,[Re^{\lambda_1 z} + (1 - R)e^{\lambda_2 z}] \tag{6}$$

where Q_S is the incident short wave radiation flux (W/m^2) at the surface, Tr and λ are the Jerlov (1976) transmission and absorption coefficients corresponding to open ocean water and they were taken as $0.62\,m^{-1}$ and $0.6\,m^{-1}$, respectively.

2.1. The Bathymetry and the Nile delta parameterization

The Egyptian Shelf Bathymetry was extracted from the U.S. Navy unclassified bathymetric database (DBDB1), which has a horizontal resolution of one minute ($1/60° \times 1/60°$). The model minimum depth was set at 2 m up to the coastline. In order to reduce the pressure gradient errors, we smoothed the model bathymetry according to the Beckman and Haidvogel "rx_0" factor (Haney, 1991; Mellor et al., 1997). This factor is given by:

$$rx_0 = |h(e) - h(e')|/h(e) + h(e') \tag{7}$$

where h(e) and h(e′) are the depths of two adjacent cells in meters, and rx_0 is a dimensionless ratio which should not go above 0.2.

We also smoothed the bathymetry by using the Laplacian filter. The model domain with the interpolated bathymetry is shown in Fig. 1. The Nile River discharge was defined by the monthly average over a 12 year-period (1975–1986) (Vörösmarty et al., 1999; Nixon, 2003) as shown in Table 1. We parameterized the outflow only through the two main branches, Rosetta and Damietta (Fig. 1). Our parameterization for the Nile River was based on a 30% reduction in discharge regarding the anthropogenic use of the river water by the population of the Nile delta. We split the total contribution into two halves for Damietta and Rosetta. We also adjusted the salinity to 10 at the two river mouths.

2.2. The atmospheric forcing

The atmospheric data for computing the surface forcing were obtained from the six-hour, 0.5° horizontal-resolution ECMWF surface analyses. The atmospheric fields used are air temperature, dew point temperature, wind velocity at 10 m above sea level, mean sea level pressure, and cloud cover. Precipitation data were obtained by interpolation of the 0.5° resolution (Legates and Willmott, 1990) climatological monthly averaged precipitation dataset. In order to parametrize the air-sea interaction processes, the wind stress, the heat fluxes and evaporation rate were computed by means of interactive bulk formulae making use of atmospheric data and the sea surface temperature predicted by the model.

The momentum flux boundary condition for the surface is:

$$\left(\rho_0 K_M \frac{\partial(u, v)}{\partial z}\right)_{z=\eta} = (\tau_{wx}, \tau_{wy}) \tag{8}$$

In Eq. (8), η is the free surface elevation in meters and τ_{wx}, τ_{wy} the wind stress components in $N\,m^{-2}$. The drag coefficient for the wind stress in Eq. (8) is computed according to Hellerman and Rosenstein (1983). The time series of the basin averaged daily mean wind stress magnitude and curl for 2006 are shown in Fig. 2(A) and (B) respectively. The wind stress magnitude shows maximum values in winter and autumn months. High frequency variability is superimposed over a seasonal cycle with maximum wind stress amplitudes of $0.25\,N\,m^{-2}$ in March. The wind stress curl is predominantly negative, therefore implying a net anticyclonic vorticity input into the basin with maximum values in late winter (end of March).

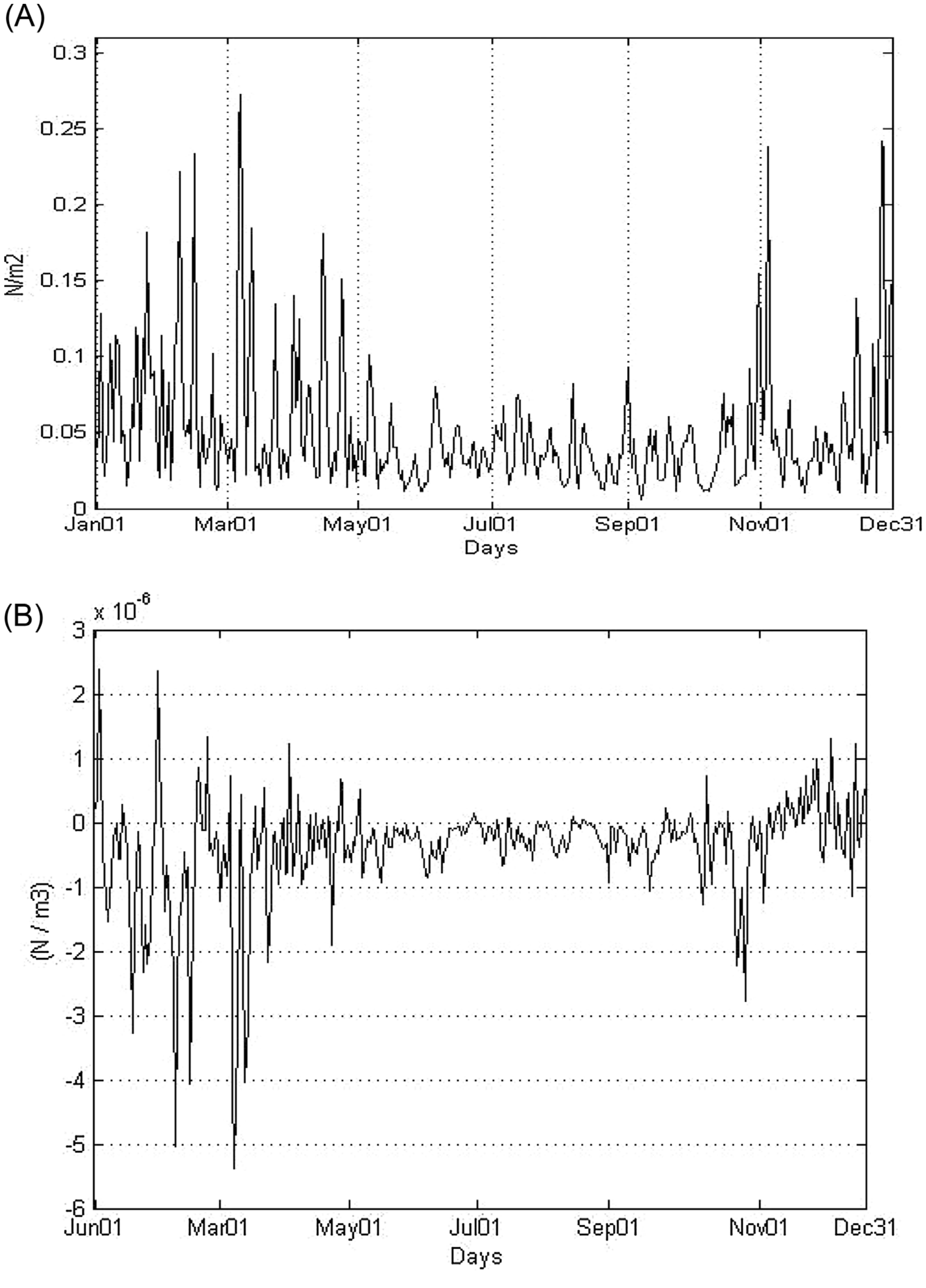

Fig. 2. Temporal evolution of the basin averaged (A) wind stress magnitude in [N/m^2] (B) wind stress curl in [N/m^3] for the model simulation period 2006.

The heat fluxes were computed interactively (Pinardi et al., 2003) and the model heat flux boundary condition is given by:

$$\rho_o C_P K_H \frac{\partial T}{\partial z}\Big|_{z=\eta} = Q_T \tag{9}$$

where Q_T is the total net heat flux according to the formula:

$$Q_T = Q_S - Q_b - Q_e - Q_h \tag{10}$$

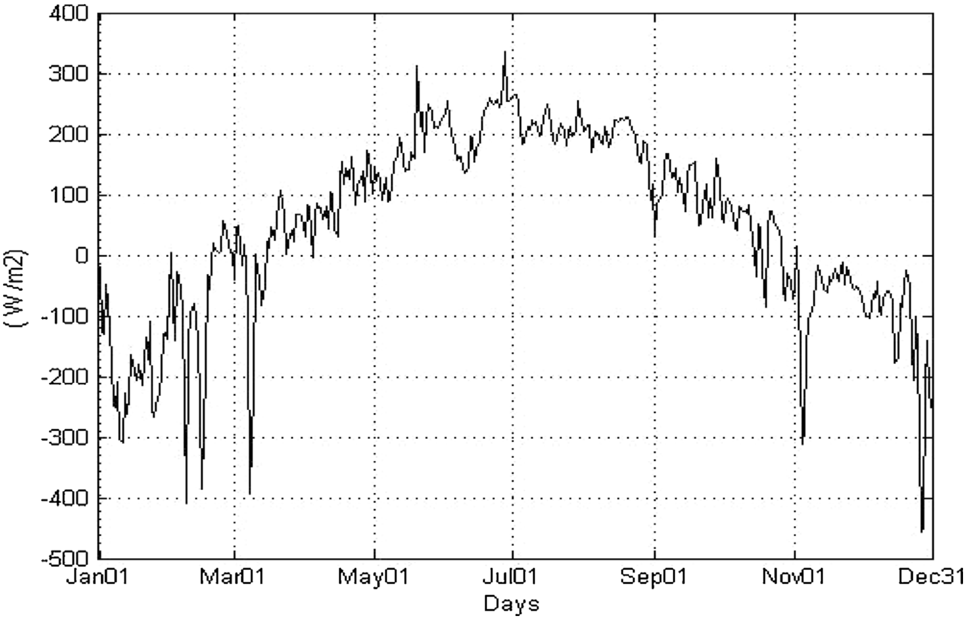

Fig. 3. Temporal evolution of the basin averaged total net heat fluxes in [W/m^2] for the model simulation period 2006.

Referring to Eq. (10) the solar radiation Qs is based on the Reed formula (Reed, 1977), as adapted by Rosati and Miyakoda (1988) for the global ocean, (Garrett et al., 1993) and (Castellari et al., 1998) for the Mediterranean region:

$$Q_S = Q_{TOT}(1 - 0.62C + 0.0019\beta)(1\text{-}\alpha) \tag{11}$$

Q_{TOT} is the total solar radiation reaching the ocean surface under a clear sky in (W/m^2), β is the solar noon altitude, α is the sea surface albedo and C is the cloud cover. Back scatter radiation Q_b at the sea surface in W/m^2 estimated by the bulk formula proposed by Bignami et al. (1995):

$$Q_b = \varepsilon\sigma T_S^4 - \left[\sigma T_A^4(0.653 + 0.00535e_A)\right].\left(1 + 0.1762C^2\right) \tag{12}$$

where ε is the sea surface emissivity taken equal to 0.97 and σ is the Stefan Boltzman constant. C is the cloud cover, e_A is the atmospheric water vapour pressure and T_s, T_A are the SST and air temperature at 2 m height above the sea surface, respectively. Q_e and Q_h are the latent and sensible heat fluxes, are computed according to the classical bulk aerodynamic formula (Rosati and Miyakoda, 1988; Castellari et al., 1998):

$$Q_e = \rho_A L_V C_E |W| \left[(e_{SAT}(T_S) - re_{SAT}(T_A)\right].\frac{0.622}{P_A} \tag{13}$$

$$Q_h = \rho_A C_P C_H |W| (T_S - T_A) \tag{14}$$

where ρ_A is the density of moist air (computed as a function of air temperature and relative humidity (r)), P_A is the atmospheric pressure, W represents the horizontal wind velocity vector at 10 m above the sea surface, e_{sat} is the atmospheric vapour pressure, C_p is the specific heat capacity of the atmospheric air, and Lv is the latent heat of vaporization calculated as a function of sea surface temperature according to Gill (1982). C_E and C_H are the turbulent exchange coefficients and both are 2.1 × 10–3 m^2 s^{-1} as proposed by Budyko (1963). The time series of the basin averaged daily mean heat flux is shown in Fig. 3. The heat flux time series shows summer maximum values (about 350 W m^{-2}) and large differences in the minima (ranging from-300 W m^{-2} in autumn up to-430 W m^{-2}) at the end of December 2006. The annual average mean value of the heat flux is −47.254 W m^{-2}.

The model water flux boundary condition follows Beron-Vera et al. (1999) considering:

$$w|z = \eta = \left(\frac{\partial\eta}{\partial t} + \vec{\upsilon}.\nabla\eta\right) + (E - P - (\frac{R}{A})) \tag{15}$$

where E is the evaporation, P the precipitation, R is the Nile River discharge, A is the river mouth cross section in m^2, and w is the vertical velocity at the free surface elevation η in meters. The corresponding salt flux boundary condition is:

$$K_H\frac{\partial S}{\partial z}|_{z=\eta} = -SSS(E - P - (\frac{R}{A})) \tag{16}$$

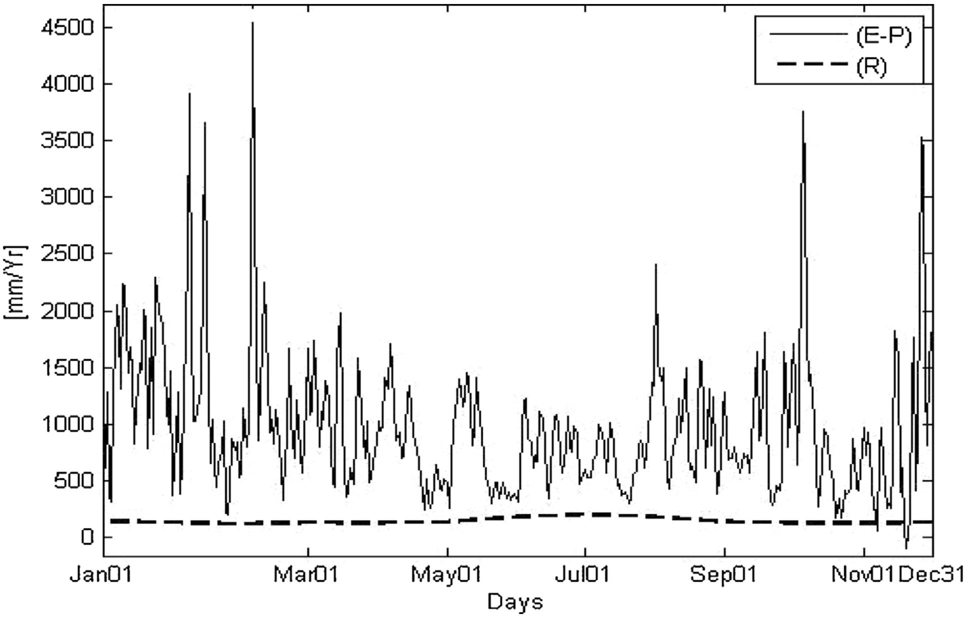

Fig. 4. Temporal evolution of the basin averaged for (E-P) (continuous line) and corresponding Nile River delta river discharge (solid dashed line) in [mm/Yr] for the model simulation period 2006.

and SSS in Eq. (15) represents the sea surface model salinity. The Egyptian Shelf Model daily mean net water flux is shown in Fig. 4 as (E-P) and R for the simulation period 2006. The Nile River contribution is about one third of the water flux budget, except in summer time (July and August) where the (E-P) values are slightly lower than the rest of the year. The discharge of the Nile River into the Mediterranean Sea is maximum, during the hot and dry summers; the government opens the high dam gates from Aswan City in order to irrigate the land and to clean the navigational channel of the Nile.

2.3. Lateral boundary conditions

Two open lateral boundaries are present north and west of our model domain (Fig. 1), where the EGYSHM is one-way nested in the MFS model. The nesting is designed to ensure that the volume transport across the open boundary of the nested model matches the volume transport of the MFS model. At the northern and western open boundaries, following Pinardi et al. (2003) and Oddo and Pinardi (2008), we impose:

$$\int_{n2}^{n1}\int_{-H_{nested}}^{\eta_{nested}} Vn_{nested}\,dzdn = \int_{n2}^{n1}\int_{-H_{nesting}}^{\eta_{nesting}} Vn_{nesting}\,dzdn \tag{17}$$

where n_1, n_2 are the extremes of the open boundary section, $\eta_{nesting}$, $H_{nesting}$ are the surface elevation and the bathymetry of the nested model, while η_{nested}, H_{nested} are the surface elevation and bathymetry of the MFS model and Vn is the normal velocity component to the open boundaries. The total tangential velocity at the open boundaries are set to be equal between the MFS and the nested model.

For the barotropic velocity we used Flather's (1976) modified boundary condition discussed in Oddo and Pinardi (2008). At the outflow we impose:

$$\overline{Vn_{nesed}} = \left[\sqrt{\frac{g}{H_{nested}}}\left(\eta_{nested}-\eta_{nesting}\right)\right] - \overline{Vn_{nesting}}\,\frac{H_{nesting}+\eta_{nesting}}{H_{nested}+\eta_{nested}} \tag{18}$$

where $\overline{Vn} = \frac{1}{H+\eta}\int_{-H}^{\eta} Vn\,dz$ is the barotropic velocity at the open boundaries and g the gravity, while at the inflow will be $\overline{Vn_{nesting}} = \overline{Vn_{nested}}$.

For the temperature and salinity, we used an upstream advection scheme whenever the normal velocity is directed outwards:

$$\frac{\partial T_{nested}}{\partial t} + Vn_{nested}\frac{\partial T_{nested}}{\partial y} = 0;\ \frac{\partial S_{nested}}{\partial t} + Vn_{nested}\frac{\partial S_{nested}}{\partial y} = 0 \tag{19}$$

On the inflow the temperature and salinity is set equal to the interpolated MFS values.

Finally, the nested model temperature and salinity fields were nudged toward the MFS values in the right hand side of the prognostic Eqs. (4) and (5), following Marchesiello et al. (2001). Denoting temperature or salinity with γ we add a relaxation term such as:

$$\frac{\partial \gamma}{\partial t} = r.h.s - \frac{1}{\Gamma}\left(\gamma - \gamma^{MFS}\right) \tag{20}$$

Here Γ is the relaxation time which varies smoothly along ten internal points of the model grid to the open boundaries, with values of 240 s–90 days. This nudging prevents the model from drifting significantly from the MFS values since the area of the high resolution nested model is small and we do not believe the fields at the boundaries should differ substantially from the MFS model solution in a one-way nested model domain.

3. The pre-operational model functioning during 2006

This section describes the procedures that are used to simulate the entire 2006 year. The nested forecasting pre-operational system works as shown in Fig. 5. The model was forced with interactive fields of momentum, surface heat, and water fluxes, which are calculated from ECMWF fields with a 6-h frequency. The chain has a daily frequency and starts with the downloading of the atmospheric fields from ECMWF. The next step is to prepare the initial and lateral boundary conditions from MFS by interpolating them into the EGYSHM grid at 1/60° horizontal resolution and 25 sigma layers. The model is in “active” mode, where it is initialized only once from MFS. The model is then run for the whole year of 2006 using the analysis and the forcing data for the entire year. The difference from a true operational forecasting system is the usage of forecast atmospheric fields and forecasted lateral boundary conditions from MFS, but overall the chain is the same.

3.1. Simulation results

This section describes the main circulation features of EGYSHM during the summer and winter of 2006. First there is a comparison between MFS and EGYSHM, and then we outline the new features captured by EGYSHM.

Fig. 6 represents the daily mean kinetic energy of EGYSHM and MFS in 2006 averaged in a vertical direction over the same region. MFS generally has larger kinetic energy amplitude peaks, with the exception of June and August 2006. The smaller energy peaks in EGYSHM are somewhat surprising given the higher resolution of the model while the larger ones could be due to the presence of river runoff in the nested model. However MFS assimilates observations (altimetric sea level, temperature and salinity profiles, Dobricic et al. (2007), and corrects toward satellite SST at the surface, as described in Tonani et al. (2008) so that kinetic energy could be larger at times due to the correction of physics uncertainties.

The near surface salinity (5 m depth) and velocity [m/s] fields in February and August are shown for both models EGYSHM and MFS in Figs. 7 and 8. The two figures also show the salinity and velocity (U,V) differences between EGYSHM and MFS with the corresponding Root Mean Square Errors. These months are chosen to represent winter and summer seasons, as described in Hecht et al. (1988). There is a significant difference between Fig. 7(A) and (B) in terms of the salinity and velocity fields. The winter fields in EGYSHM are characterized by more energetic circulation patterns, with a relatively low salinity band near the Nile Delta outflows where the salinity can reach 10 PSU especially in front of the two Nile River mouths. In addition EGYSHM shows a well-defined Mersa-Matruh gyre in the western part of the domain, much stronger than MFS. The along-slope eastward flow field entering the domain around 33° 40′ N encircles seaward the Mersa-Matruh gyre in EGYSHM, while in MFS it cuts the anticyclonic gyre into two smaller eddies, around 32° N. The finer model resolution and the better Nile River runoff of EGYSHM produce this change. The salinity differences between the two models is maximum in front of the Nile Delta as shown in Fig. 7(C), while the monthly basin averaged RMSE between the models is only 0.244 PSU. The maximum differences between east and north velocity components for the two models are about ±0.2 m/s as shown in Fig. 7(D) and (E). The location of these maximum differences is at the western domain from 26 to 30° N. Another large area of differences is to the southeast of the model domain, lying between 31 and 34° E and from 31 to 32° N. We believe that this area represents the Nile plume which flows eastward to the Egyptian Coast. It seems that the main reason for the underestimated salinity along the Egyptian coast is due to initialization by low salinity at river mouths at 10 PSU. The monthly basin averaged of the RMSE for U and V velocity components differences from both models are 0.136 and 0.1064 m/s, respectively.

Fig. 8(A) presents the EGYSHM summer 2006 circulation: the Mersa-Matruh gyre is now shifted westward and it is made up of several anticyclonic lobes, forming the Mersa-Matruh gyre system, covering an area between (25.5–32° E), in agreement with Korres and Lascaratos (2003). Note the differences in the salinity and circulation fields between EGYSHM and MFS, as shown in Fig. 8(C)–(E). EGYSHM has richer and better defined mesoscale structures when compared with MFS, localized around the meandering of a surface current which develops in the open ocean area west of the Nile delta and then hugs the shelf slope area. Fig. 8(D) reports the difference in the east velocity component between EGYSHM and MFS. In MFS the currents only develop on the shelf slope and they are weaker than in EGYSHM, as shown in Fig. 8(D). In August the salinity of EGYSHM is lower than MFS in front of the Nile delta region but it is slightly higher in the rest of the domain, see Fig. 8(B) and (C). This is due to the particular surface flux parameterization of MFS which, as explained in

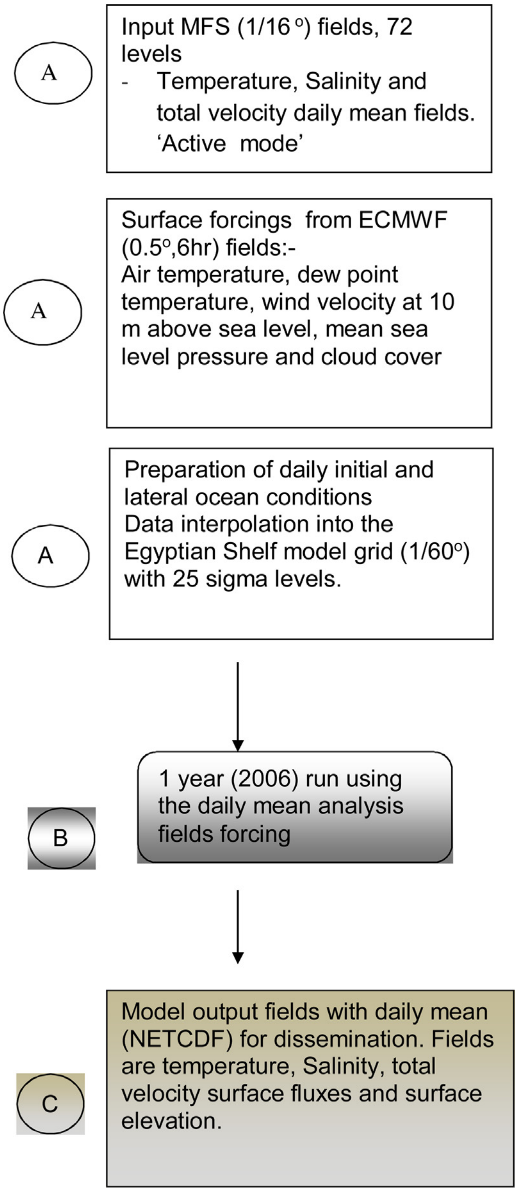

Fig. 5. Pre-operational functioning for the Egyptian Shelf Model during the simulation period of 2006.

Tonani et al. (2008), introduces a low salinity bias everywhere in the MFS model domain. The RMSE basin averaged between EGYSHM and MFS for the salinity, east and north velocity components are 0.34, 0.13 m/s and 0.1171 m/s respectively.

The February and August structure of the circulation in this area is characterised by a one ocean/shelf slope current, which we call the Egyptian Shelf Slope Current (ESSC). This current meanders around the Mersa-Matruh gyre system in August and February, and also carries the low salinity waters, i.e. Modified Atlantic Water-MAW (POEM Workshop, 1989; POEM Group, 1992; Malanotte-Rizzoli et al., 1997) into the region.

In order to gain better insight into the circulation structure of the EGYSHM solution, two different meridional sections taken at longitude 32° and 26.5° E are shown in Figs. 9 (A), (B), 10 (A), (B), 11 (A), (B) and Fig. 12(A), (B). The 32° E meridional section represents the cross-shelf domain downstream of the Damietta outflow (Fig. 1) while the 26.5° E shows the cross-shelf domain cutting the ESSC. The salinity field is overlaid to the northward and the eastward velocity components displayed as contour lines.

There are clear differences between February and August for both velocity contours and salinity distributions along the eastern transect, as shown in Figs. 9(A,B) and 10(A,B). Positive eastward velocities [0.2 m/s] are large with weak negative northward velocities [−0.04 m/s] suggesting a dominant eastward ESSC direction. EGYSHM suggests two core structures for the ESSC during August while in February, the ESSC is weaker [0.12 m/s] and is shifted further offshore in a homogeneous

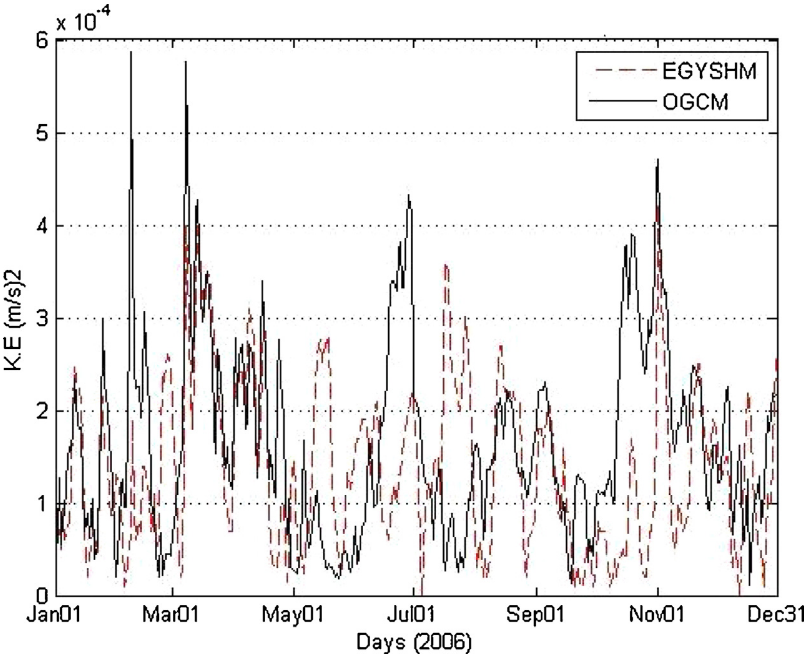

Fig. 6. Temporal evolution of the basin averaged for MFS kinetic energy (continuous line) and corresponding Egyptian Shelf Zone kinetic energy (dashed line) in [m^2/s^2] for the model simulation period 2006.

layer from surface to 50 m depth. The offshore extension of the ESSC is bounded by the extension of a cyclonic circulation region occupying the region starting from 32° N. The effect of the Nile on the salinity distributions for both seasons is very clear as highlighted in Figs. 9 and 10. This effect is limited to the shelf area in both seasons, but during winter it extends further offshore partly producing lower salinities in February than in August.

In the western transect, shown in Figs. 11 and 12, the eastward velocity component contour demarcates the ESSC upstream of the Mersa-Matruh gyre system. The maximum ESSC eastward velocity value is [0.3 m/s], recorded in August around 32.8–33° N, extending down to 500 m, see Fig. 11(A). On the shelf slope, a westward current develops, contrary to the ESSC. Fig. 11(A) clearly indicates the presence of LIW between latitudes and depths of 31.6–31.8° E, 200–400 m respectively, where the averaged salinity is 38.9. Fig. 12(A) highlights that the Mersa-Matruh gyre system is well developed and larger in August than February (Fig. 11A), covering the area from 32.3–33.1° N.

3.2. Sensitivity studies

In order to understand the effects of wind stress in the model solutions we carried out an experiment (EGYSHM2) without wind stress – the results are shown in Figs. 13 and 14).

The two simulated February months in Figs. 7(A) and 13(A) are characterized by a well-defined Mersa-Matruh gyre. The differences between the two simulations [EGYSHM-EGYSHM2] are also shown for the east and north velocity components (Fig. 13B and C) with their corresponding RMSE. EGYSHM shows a larger gyre than EGYSHM2, but the Mersa-Matruh gyre is clearly dominated by all the other forcings, in particular the heat forcing in agreement with Roussenov et al. (1995) and Korres et al. (2000).

There is an interesting difference between the February cases with and without winds in the salinity field. Nile River water extension in EGYSHM2 is further offshore and the salinity is generally lower than EGYSHM. This can be attributed to the weaker ESSC due to a direct effect of the wind stress absence but also to the indirect effect of lower vertical mixing due to the absence of turbulent kinetic energy inputs in the Mellor-Yamada scheme.

Figs. 8(A) and 14(A) show the August salinity and velocity near surface (5 m depth) fields for EGYSHM and EGYSHM2, respectively. Fig. 14(B) and (C) show the velocity components differences between the two simulations with their basin averaged RMSE. A significant difference can be noted between the two fields. The EGYSHM2 salinity field has higher salinity values covering most of the domain except in front of the Nile Delta region. This can be explained by the weaker surface currents – see Fig. 14(B) and (C) – which transport less MAW into the Egyptian areas.

EGYSHM2 shows a well-defined El-Arish gyre which is almost absent in the EGYSHM simulation. The weaker ESSC in EGYSHM2 has a very clear impact on the salinity distribution along the Nile Delta, leaving two large low salinity plumes in front of the Rosetta and Damietta outflows. This weak ESSC in EGYSHM2 is clear in Fig. 14(B) and (C) from the increase in the

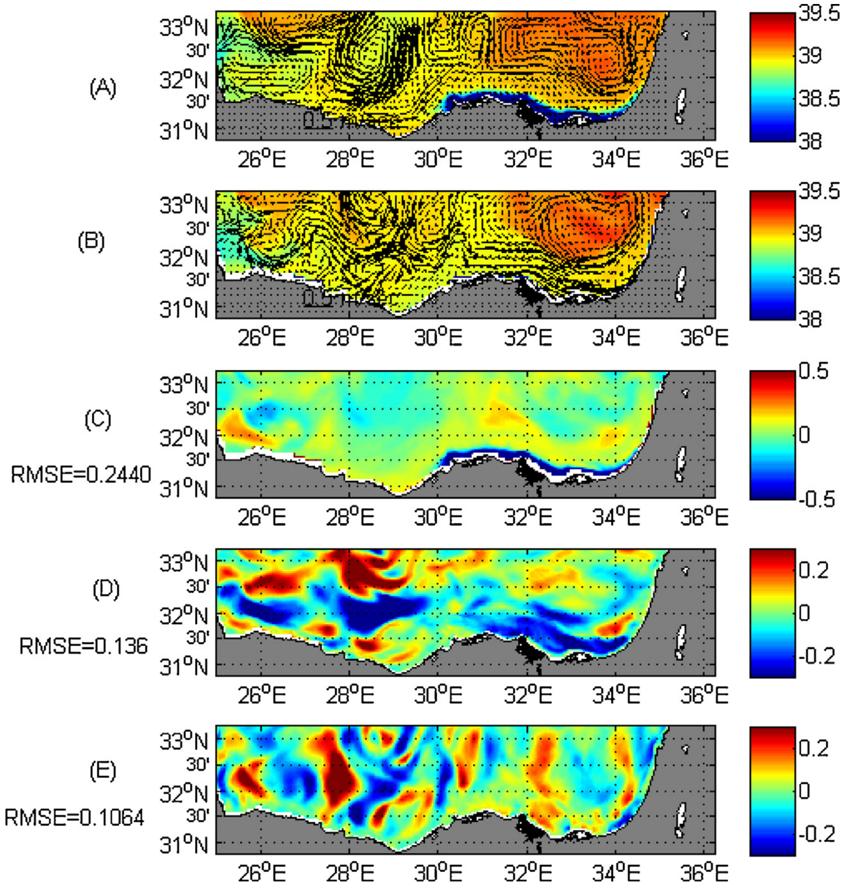

Fig. 7. (A) Near surface salinity (5 m depth) and velocity [m/s] fields for February 2006; (B) MFS model; (C) Salinity differences between EGYSHM and MFS; (D) Velocity component U differences between EGYSHM and MFS; and (E) Velocity component V differences between EGYSHM and MFS, with their mean averaged RMSE.

RMSE between the two simulations, which have reached 0.13 and 0.11 m/s, respectively. Overall, the role of the momentum flux is crucial in reproducing a strong ESSC.

4. Validation/calibration with observations

In this section, we validate the EGYSHM temperature, salinity and sea surface height (SSH) with observations. The observations are sea surface temperature (SST) from satellite data in 2006, temperature and salinity profiles from ARGO floats in March 2006 and sea level anomaly (SLA) from satellite data.

4.1. Comparison between EGYSHM and NOAA-AVHRR SST during the simulation period

Available observations in the Egyptian Shelf Zone for the simulation period were daily objectively analyzed satellite SST computed from night-time NOAA-AVHRR-14 and NOAA AVHRR-15 satellites (Buongiorno Nardelli et al., 2003; Marullo et al., 2007).

We removed all SST-data points where the error is more than 10% from the objective mapping, i.e., where large cloud gaps were filled by the interpolation. Table 2 shows the monthly basin averaged mean, correlation coefficient and RMSE between EGYSHM SST and NOAA-AVHRR SST and Fig. 15 shows the daily mean basin averaged time series for the EGYSHM SST and the corresponding satellite SST. The highest monthly mean difference was about 1.2 °C and was recorded in April 2006. The lowest difference mean was [−0.1733 °C] in November. The SST from the EGYSHM is warmer than satellite during most of the year months except June, July, October, November and December when the EGYSHM SST is cooler. This may be due to the model atmospheric forcing uncertainties during these months. In general the EGYSHM SST is significantly correlated to satellite SST in all months at a 95% confidence limit. The highest correlation coefficient was 0.9743 for May 2006. The minimum correlation coefficient was 0.16 for February. We know that February has the largest satellite SST data error points because of cloud cover. For the RMSE, the highest value was 1.03 °C in June, while the lowest one was 0.551 °C in August 2006. This model error is clearly due to the model air-sea physics parametrizations used in EGYSHM which are similar to

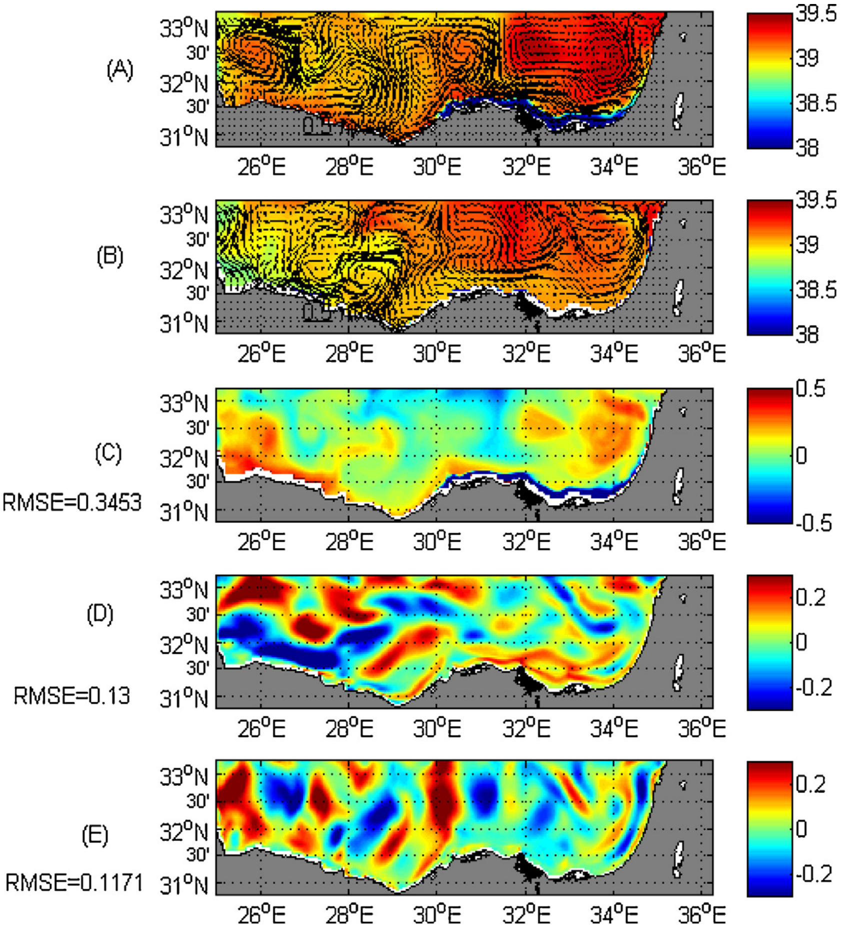

Fig. 8. (A) Near Surface salinity (5 m depth) and velocity [m/s] fields for August 2006; (B) MFS model; (C) Salinity differences between EGYSHM and MFS (D) Velocity component U differences between EGYSHM and MFS; and (E) Velocity component V differences between EGYSHM and MFS, with their mean averaged RMSE.

Table 2
Monthly basin averaged differences for the mean in [°C], correlation coefficients and RMSE [°C] between EGYSHM and AVHRR SST during the model simulation period for the year 2006.

Month	SST mean basin averaged differences between EGYSHM and satellite SST [°C]	Correlation coefficient between EGYSHM and satellite SST (all are significant at 95% confidence limit)	RMSE between EGYSHM and satellite SST (°C)
January	0.1942	0.9593	0.783
February	0.6753	0.166	0.5617
March	1.1413	0.3861	0.6917
April	1.2924	0.2632	0.6124
May	0.7478	0.9743	0.613
June	−0.2357	0.8907	1.0378
July	−0.4069	0.6812	0.7262
August	0.2689	0.6601	0.5551
September	0.412	0.575	0.6512
October	−0.2607	0.9108	0.7929
November	−0.1733	0.9638	0.9297
December	−0.2054	0.9641	0.8094

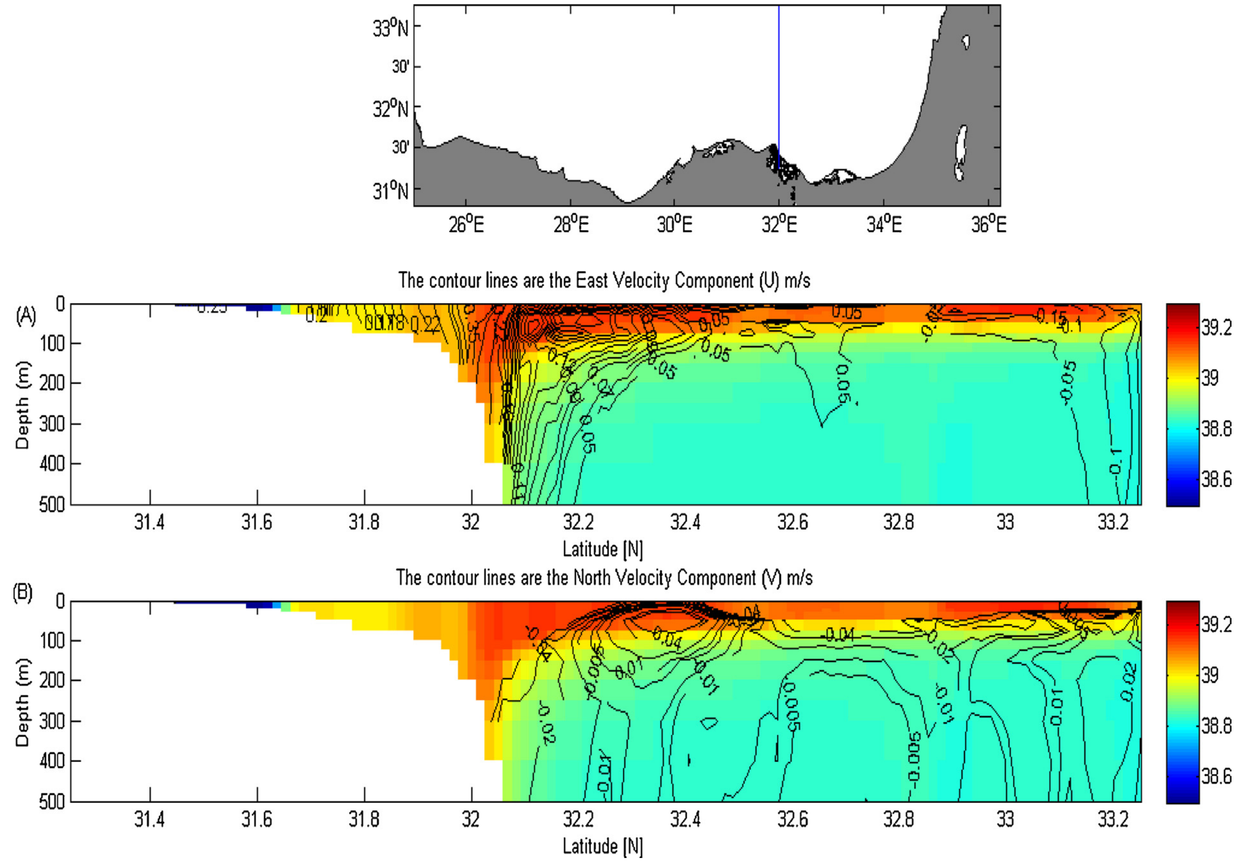

The contour lines are the East Velocity Component (U) m/s

The contour lines are the North Velocity Component (V) m/s

Fig. 9. Meridional cross section in February 2006 at longitude 32° E for the salinity field, eastward and northward velocity components shown as black contours [m/s] for the EGYSHM: (A) Salinity field with the eastward velocity component (U); (B) Salinity field with the northward velocity component (V).

MFS. This error is discussed at length by Tonani et al. (2009) and Pettenuzzo et al. (2010) who analyse the atmospheric forcing uncertainties giving rise to model errors.

4.2. Comparison of Argo temperature and salinity profiles with the EGYSHM results in March 2006

A meridional section was chosen to cover the Egyptian Shelf water at longitude 26°E, as shown in Figs. 16 and 17A, B and C for the temperature and salinity in March. Our spatial and temporal selection was based on the best Argo profiles data coverage for our domain during the whole simulation period in 2006. The Mediterranean Argo data program is described in Poulain et al. (2007), Manzella et al. (2003) and Tonani et al. (2009).

Fig. 16(A and B) show the same cross section with results of EGYSHM and Argo profiles that were taken in March 2006. Fig. 16(C) shows the difference between the model and Argo float profiles data and its RMSE. There is a significant resemblance in the temperature patterns between the Argo data and the model in the upper and lower 100m. On the other hand there are two clear differences. The first is that the Argo floats data have more diffused and deeper thermocline layer, more than 100 m, while the model shows a thermocline at about 50 m depth. The larger thickness of the upper layer, recorded by the Argo floats, is probably due to the active vertical mixing in March, that is associated with water mass formation processes. The model is not capable to reproduce the heat losses capable to start such mixing and the mixed layer is left unchanged from the autumn. In support of this conjecture, Fig. 16(C) shows more than 1 °C higher temperature in EGYSHM than the Argo data in the upper 50 m. The RMSE difference between the model temperature and Argo data was about 0.9 °C averaged over the section.

In Fig. 17A–C we used the same section as above for the salinity comparison. The EGYSHM was unable produce a well-defined LIW probably due to excessive mixing processes. In general, the EGYSHM has a lower salinity than Argo salinity data with maximum difference of around 0.1, as shown in Fig. 17(C). The salinity averaged RMSE between EGYSHM and Argo data is about 0.09.

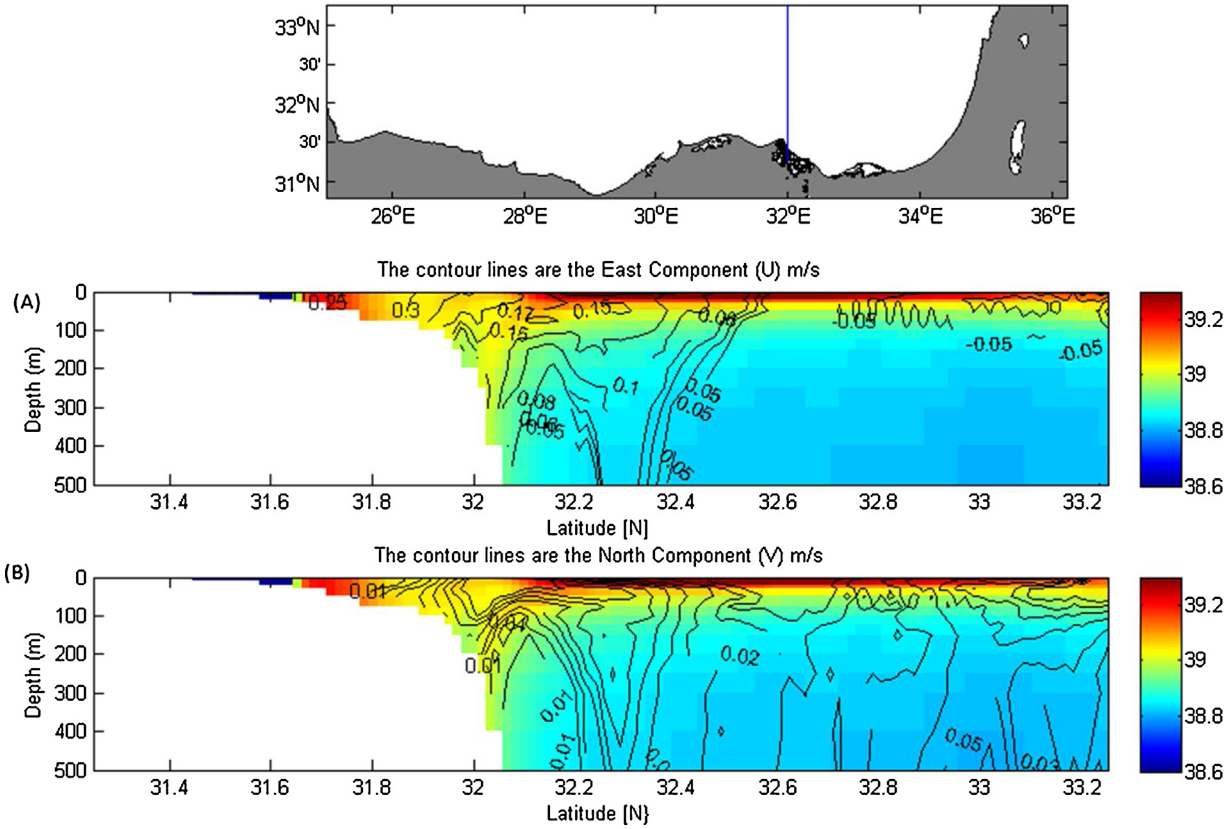

Fig. 10. Meridional cross section in August 2006 at longitude 32° E for the salinity field with eastward and northward velocity components shown as black contours [m/s] for the EGYSHM: (A) Salinity field with eastward velocity component (U); (B) Salinity field with northward velocity component (V).

4.3. *Comparison between EGYSHM (SSH) and SLA from satellite during the year 2006*

The SLA data are monthly means covering the whole Mediterranean Sea with a horizontal resolution of 0.25° in latitude and longitude from AVISO. Our aim was to compare model results with satellite altimetry to verify the positions and the shape of the mesoscale eddies identified/simulated by the EGYSHM model.

Fig. 18A–C shows February 2006, EGYSHM SSH, SLA from satellite with the difference between them, and the corresponding RMSE. Note the resemblance between the two maps in the position and the shape of the Mersa-Matruh anticyclone gyre feature, which occupies the area between 27 and 28.5° E. EGYSHM has a small shift to the east in positioning the Mersa-Matruh gyre system. There is another similarity in the mesoscale feature, which is located at 31° E and 33° N. There are two differences between the two maps, as shown in Fig. 18(C). The first difference is located in the east of the domain between 32–34° E and the other one is at 25.5° E. This may be due to using the model SSH without removing the MDT.

Fig. 19A–C showings the SSH and SLA models with the difference between them during November 2006. Fig. 19(A) and (B) highlight some similarities in positions and shapes of mesoscale features. There is some matching between Fig. 19A and B in the western domain from 25.5–28° E which is occupied by the Mersa- Matruh feature. Again, the difference is observed at the eastern part of the domain for the same reason mentioned above.

Table 3 shows the averaged RMSE between models SSH and SLA from satellite. All the RMSE values are less than 0.07 m with a minimum of 0.03 m in November. The RMSE values shown in Table 3 reveal the robustness of EGYSHM SSH. This may be due to the fact that EGYSHM is provided with water flux boundary conditions (see Section 2).

5. Conclusions

This paper describes for the first time a nested pre-operational model for the Egyptian shelf zone. This is a basic dynamical study that shows the capability of the nested model to reproduce the known structures of the circulation with realistic atmospheric forcing. The model is forced by lateral boundary conditions taken daily from the MFS model and atmospheric interactive fluxes calculated from 6 h ECMWF surface fields. The model was run in ‘active’ mode. The vorticity input by the wind in the basin is largely negative, which explains the anticyclonic activity of the area. The heat fluxes are negative as well as the water budget, as expected.

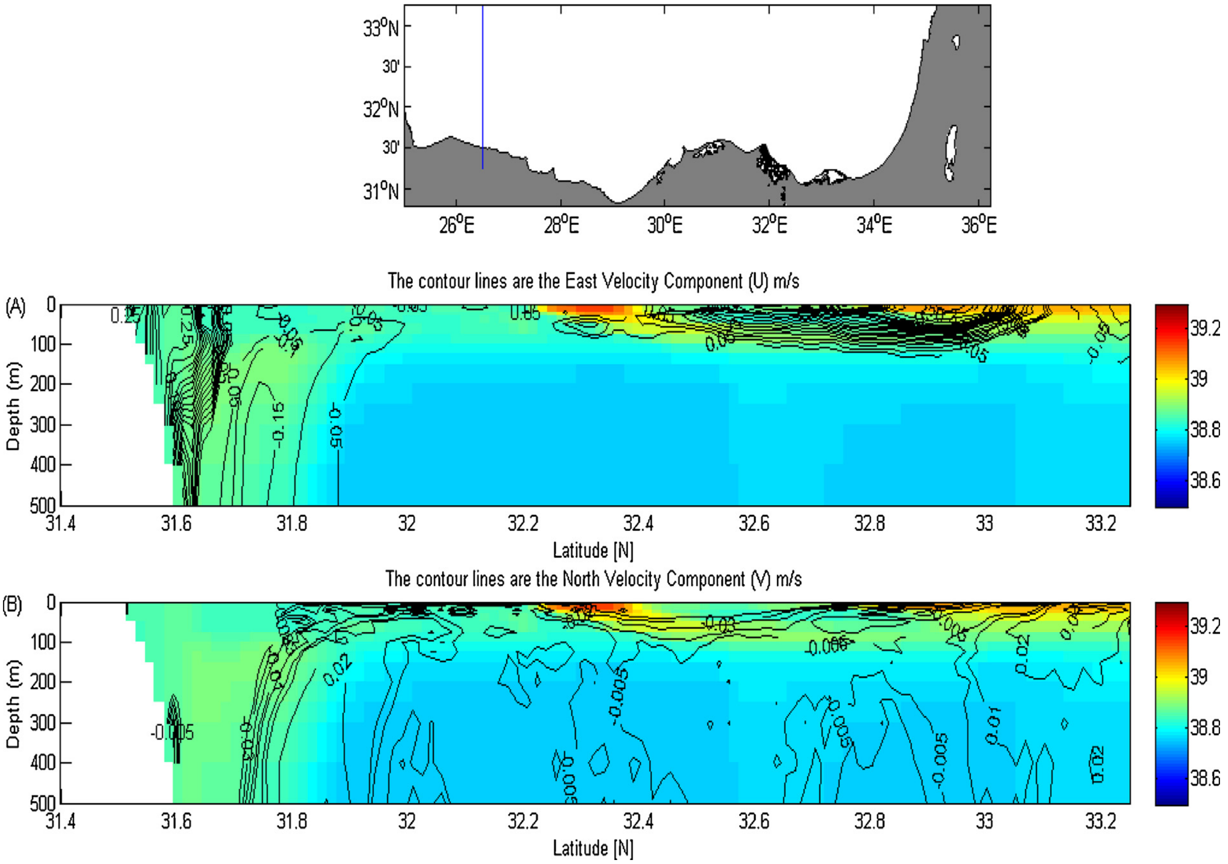

Fig. 11. Meridional cross section in February 2006 at longitude 26.5° E for the salinity field with eastward and northward velocity components shown as black contours [m/s] for the EGYSHM. (A) Salinity field with eastward velocity component (U); (B) Salinity field with northward velocity component (V).

Table 3
Monthly basin averaged RMSE between EGYSHM (SSH) and SLA from satellite during the model simulation period for the year 2006 in meters.

Month	RMSE between EGYSHM SSH & Sea Level Anomaly from satellite in meters
January	0.06
February	0.06
March	0.06
April	0.06
May	0.07
June	0.07
July	0.06
August	0.07
September	0.05
October	0.04
November	0.03
December	0.06

EGYSHM reproduces the main region circulation patterns, adding the dynamics forced by the Nile River outflow. The winter fields in EGYSHM are characterized by energetic circulation patterns, with a relatively low salinity band in the Nile Delta shelf and a well-defined Mersa-Matruh gyre. The simulation suggests the presence of an Egyptian Shelf Slope Current (ESSC) which flows eastward at different depths in the domain. The ESSC at the western part of our domain runs offshore in the western part of the domain while in the easternmost part it hugs the shelf slope at about 300 m. We found that in February 2006 the salinity difference between the two models [MFS and EGYSHM] was maximum in front of the Nile Delta, as shown in Fig. 7(C). The monthly mean basin averaged RMSE between the two models was 0.244 PSU, while the maximum velocity components differences between the two models are about ±0.2 m/s.

In the August circulation, the Mersa Matruh gyre system is defined by three lobes, and covers an area between (25.5–32° E) in agreement with Korres and Lascaratos (2003). The ESSC is stronger and more defined in August than February. The RMSE basin averaged between EGYSHM and MFS in August 2006, for the salinity, eastward and northward velocity components were 0.34, 0.13 m/s and 0.1171 m/s respectively.

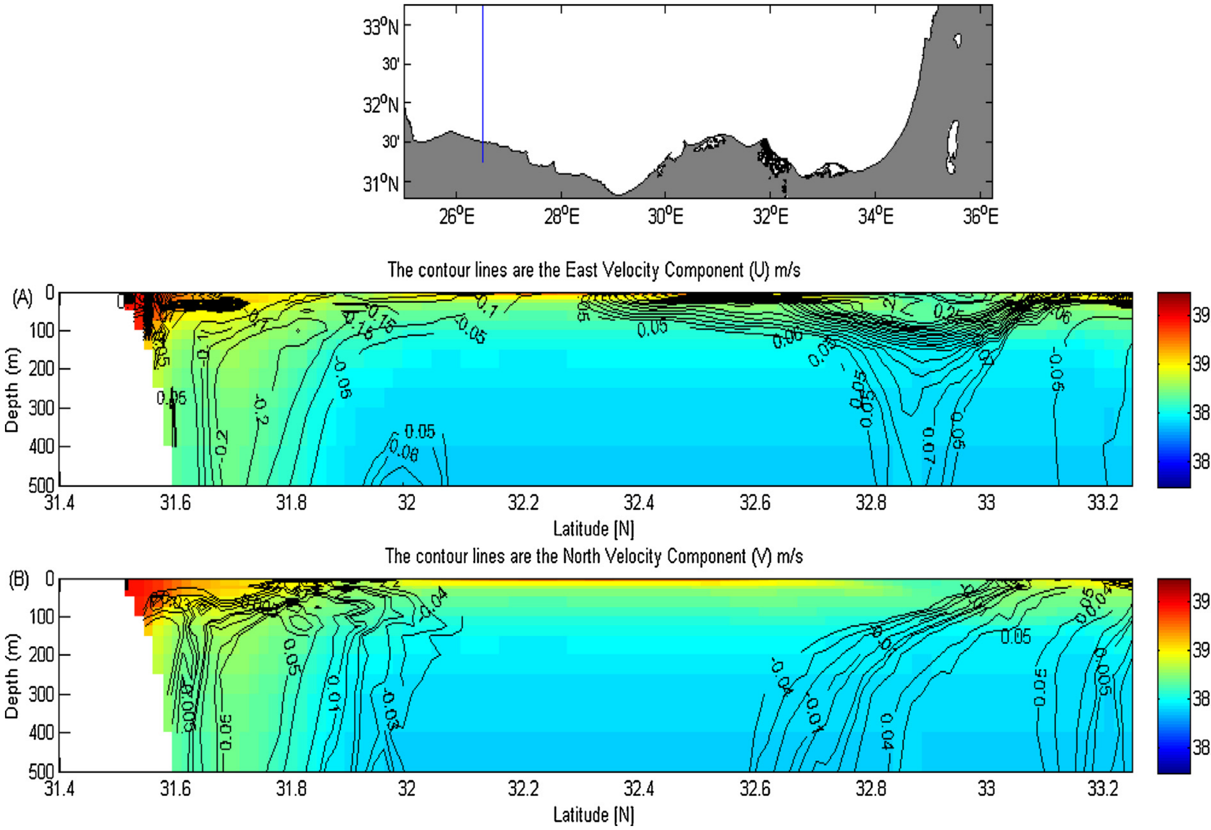

Fig. 12. Meridional cross section in August 2006 at longitude 26.5° E for the salinity field with eastward and northward velocity components shown as black contours [m/s] for the EGYSHM. (A) Salinity field with eastward velocity component (U) (B) Salinity field with northward velocity component (V).

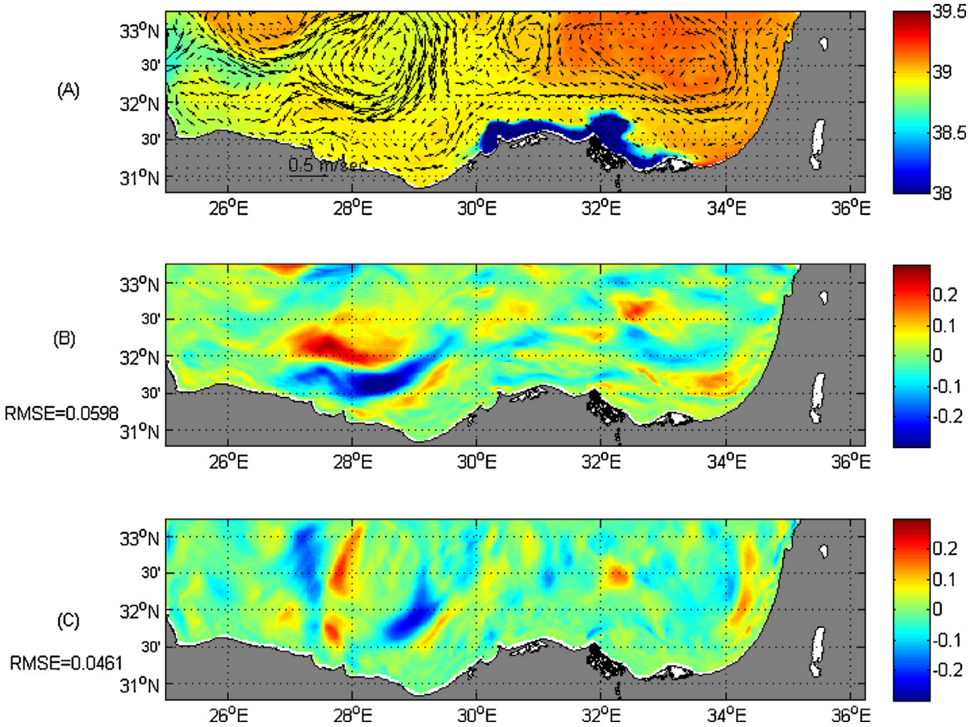

Fig. 13. February 2006: (A) Near Surface (5 m depth) velocity [m/s] and salinity fields for the EGYSHM2, (B) Eastward velocity component difference between the EGYSHM and EGYSHM2 (C) Northward velocity component difference between the EGYSHM and EGYSHM2 with their mean averaged RMSE.

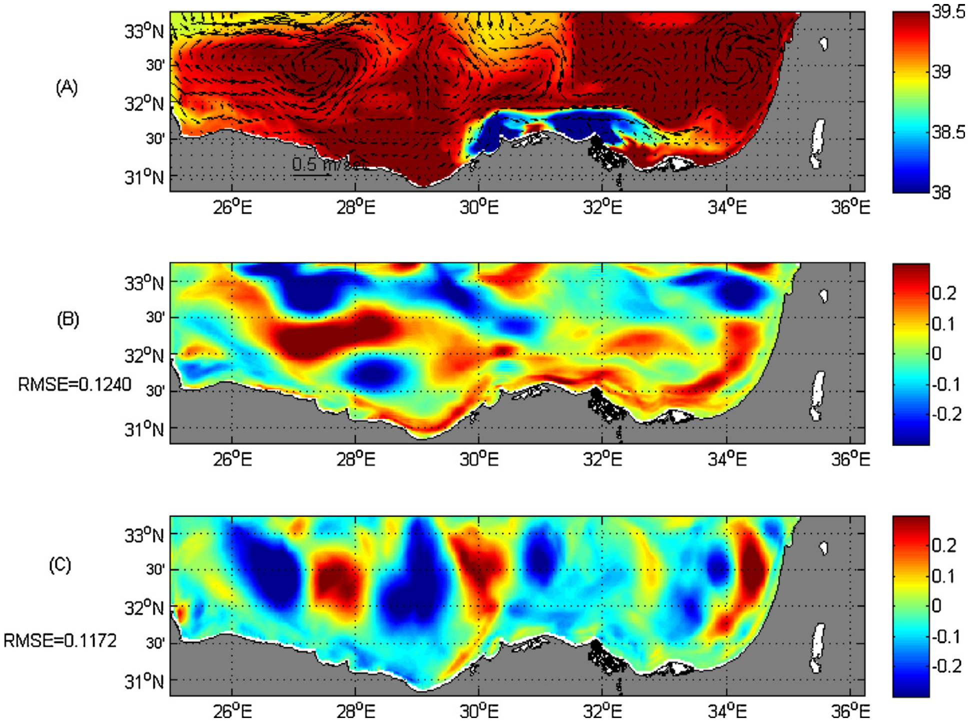

Fig. 14. August 2006: (A) Near Surface (5 m depth) velocity [m/s] and salinity fields for the EGYSHM2, (B) Eastward velocity component difference between the EGYSHM and EGYSHM2 (C) Northward velocity component difference between the EGYSHM and EGYSHM2 with their mean averaged RMSE.

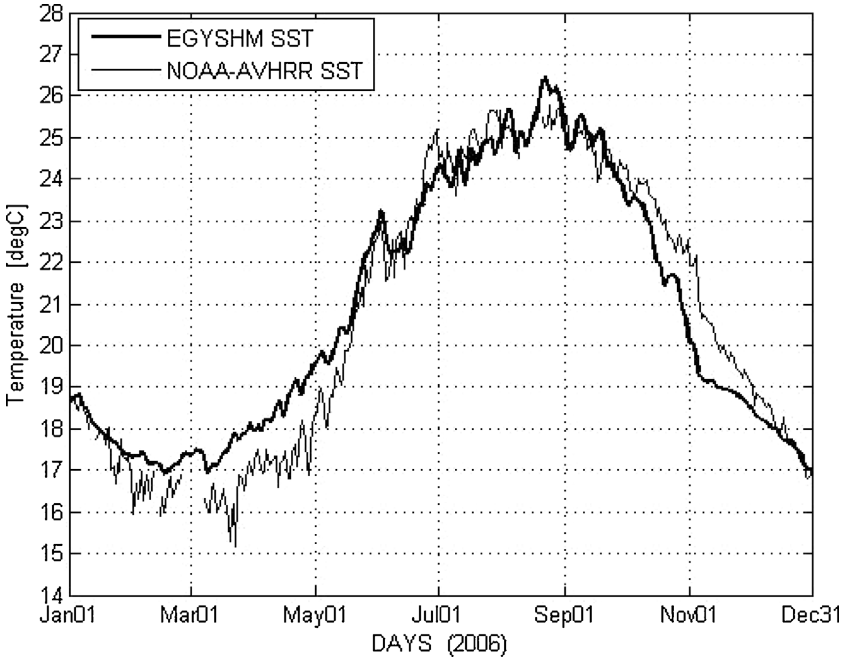

Fig. 15. Temporal evolution of the basin averaged for EGYSHM SST (continuous thick line) and corresponding AVHRR SST (thin line) in [°C] for the 2006 period.

EGYSHM is also characterized by a well-defined MAW (Modified Atlantic Water) signal in all seasons, at the surface in February and at depth in August.

Two different meridional sections were carefully studied. The northward velocity components were weak [0.04 m/s] in these longitudinal sections and the flow direction is mainly composed of the eastward velocity component. The maximum eastward component velocity of the ESSC [0.25 m/s] is located near the continental slope during the summer time while, in

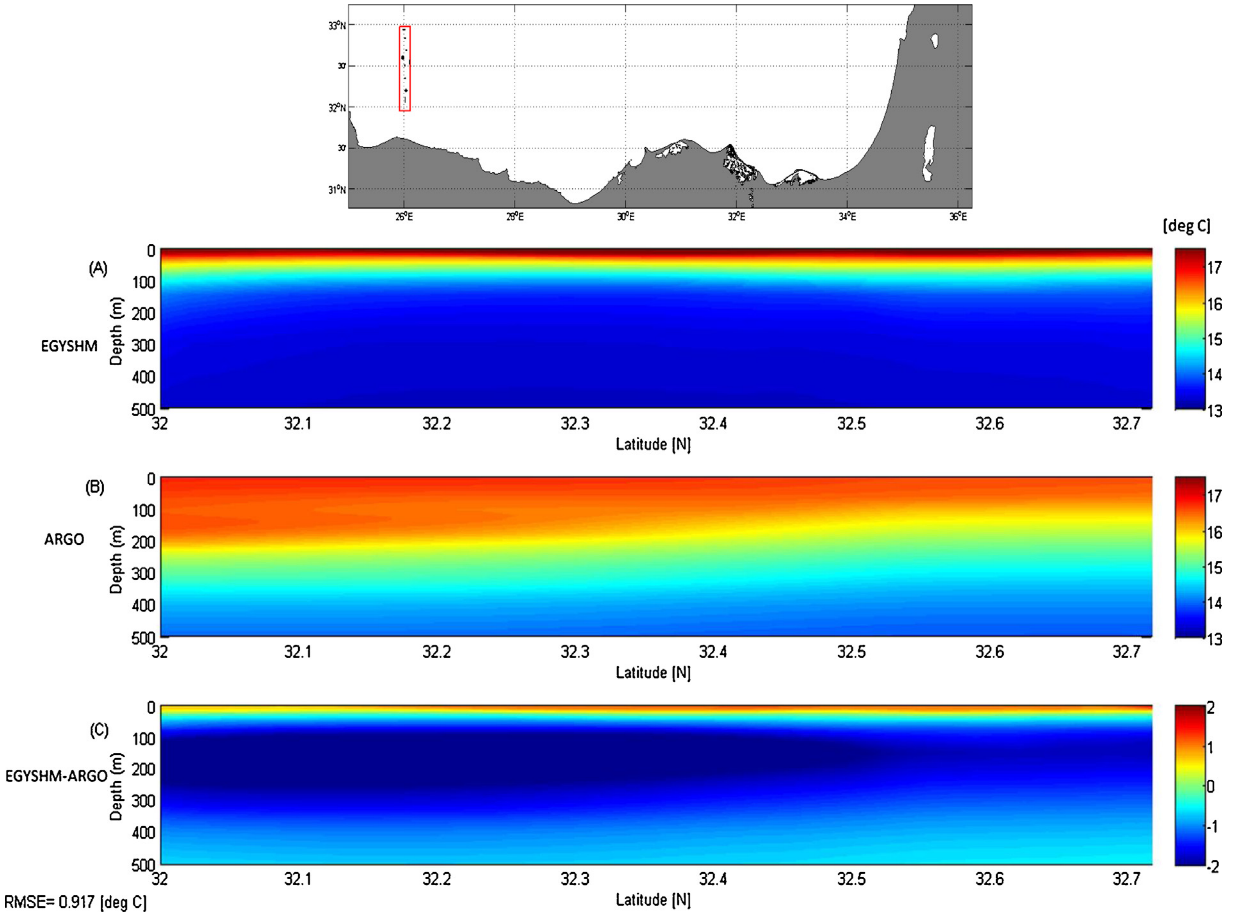

Fig. 16. Meridional temperature cross section in March 2006 at longitude 26° E [°C] (A) for EGYSHM, (B) for Argo profiles (C) and the difference between EGYSHM and Argo, with the corresponding RMSE.

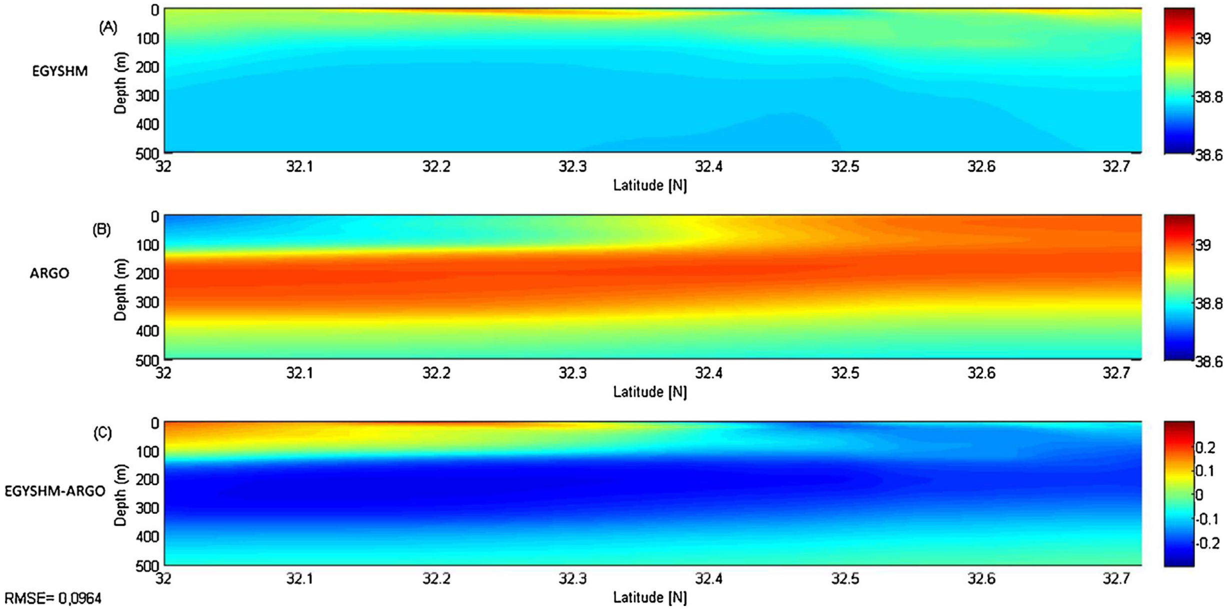

Fig. 17. Meridional salinity cross section in March 2006 at longitude 26° E [°C] (A) for EGYSHM, (B) for Argo profiles (C) and the difference between EGYSHM and Argo profiles, with the corresponding RMSE.

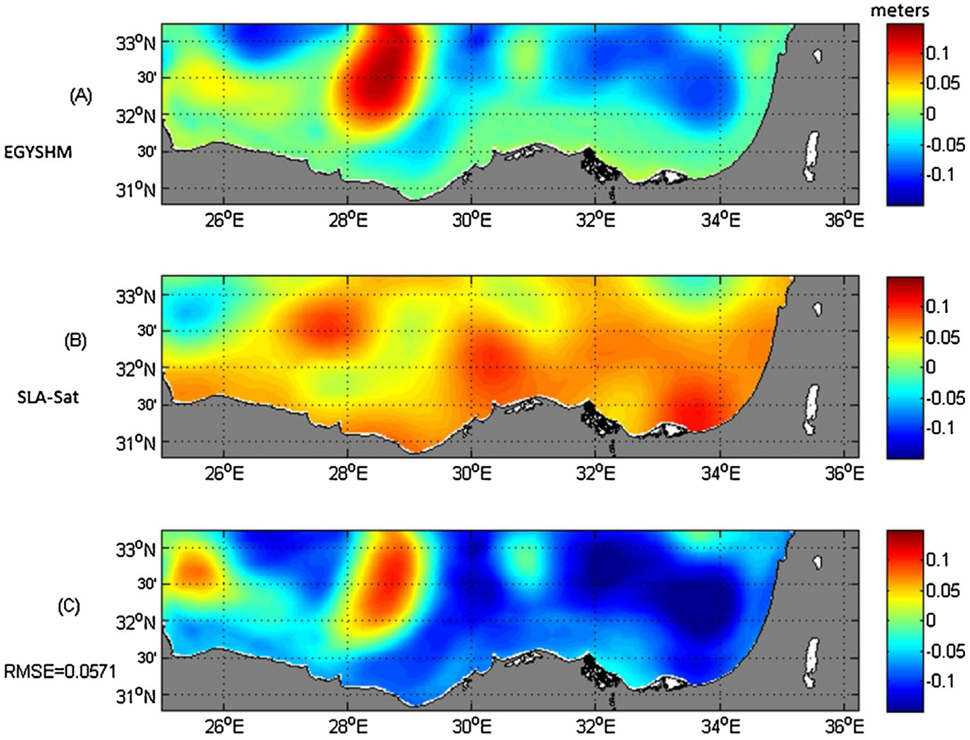

Fig. 18. (A) Monthly Sea Surface Height averaged for the EGYSHM in February 2006 (m) (B) Monthly averaged Sea Level Anomaly averaged from Satellite February 2006 (m) (C) the difference between EGYSHM SSH and SLA, with the corresponding RMSE.

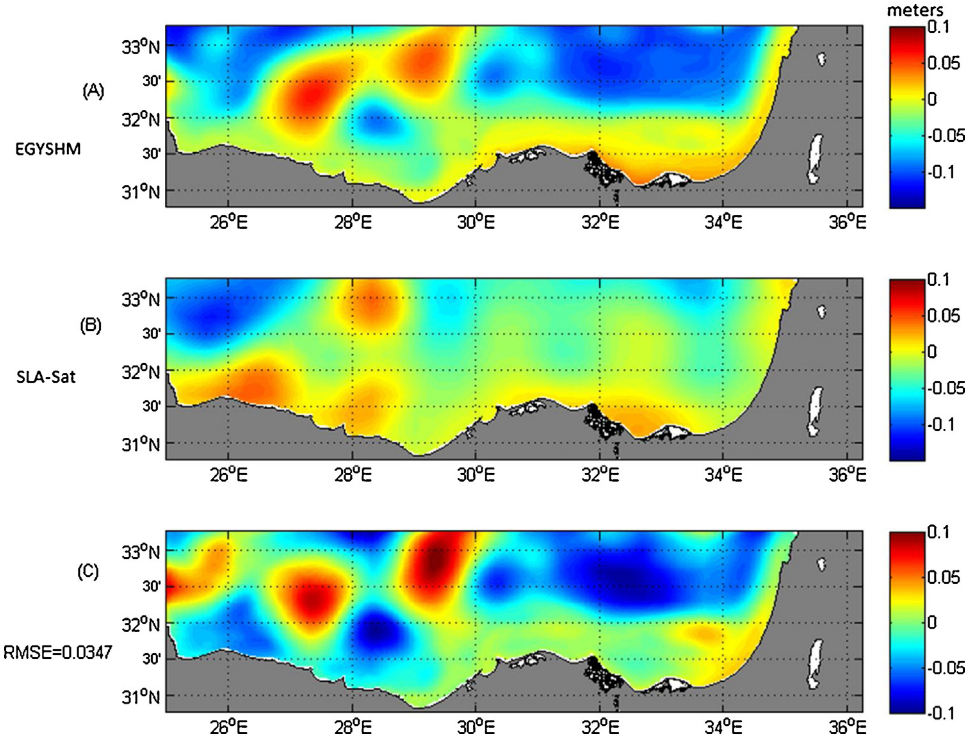

Fig. 19. (A) Monthly Sea Surface Height averaged for the EGYSHM in November 2006 (m) (B) Monthly averaged Sea Level Anomaly from satellite data in November 2006 (m) (C) the difference between EGYSHM SSH and SLA, with the corresponding RMSE.

winter the ESSC is weaker [0.04 m/s]. The ESSC is directly affected by the Mersa-Matruh gyre system, which intensifies in summer time.

The effect of the Nile River is strongest on the shelf in both seasons and it extends further offshore during February, probably mixing with the MAW surface waters. The western transect shows that the Mersa-Matruh gyre is larger and stronger in summer than winter. The maximum velocity of the gyre is [0.3 m/s]. This gyre is visible up to 500 m depth in summer. Mersa-Matruh shows a large seasonal cycle in strength, reaching a maximum amplitude during summer, in agreement with Roussenov et al. (1995); Korres and Lascaratos (2003). In February 2006, in the western transect we observed a clear sign for the LIW between latitudes 31.6–31.8 °E and depths of 200 and 400 m, respectively, with an averaged salinity of 38.9 in agreement with POEM Workshop (1989); POEM Group (1992), and Malanotte-Rizzoli et al. (1997).

The role of wind stress on the dynamics of the area is crucial in terms of forcing the circulation of the Egyptian shelf. ESSC is weaker when wind stress is neglected in EGYSHM2 and as a consequence the Nile River waters extend further offshore. In August 2006, the RMSE between the two simulations increased and reached 0.13 and 0.11 m/s for the east and north velocity components, respectively.

The comparison with all available observations highlighted that the model is relatively capable to reproduce the thermal structures of the field in the area. The comparison of the satellite SST with the model shows a good agreement, similar to the one of many other operational systems (Tonani et al., 2009). The SST for the EGYSHM was warmer than the satellite data during most of the year months except June, July, October, November and December where the EGYSHM SST was cooler. This may be to the model atmospheric forcing uncertainties during these months. The highest correlation coefficient was 0.9743 in May 2006. The minimum correlation coefficient was 0.16 and was obtained for February. Most of the RMSE values between EGYSHM SST and NOAA-AVHRR SST were less than 1 °C except for June 2006.

We compared Argo temperature and salinity profiles with the EGYSHM results in March 2006. There was a significant resemblance in the temperature patterns between the Argo data and the model in the upper and lower 100 m depth. EGYSHM reported a higher temperature (more than 1 °C) than the Argo data in the upper 50 m). The averaged RMSE between the model temperature and Argo data was about 0.9 °C. The EGYSHM managed to produce a well-defined MAW, as contained in the Argo profiles but not the LIW layer probably because the model is affected by excessive mixing. In general, the EGYSHM gave lower salinity values than Argo, with a maximum difference around 0.1 as shown in Fig. 16(C).

We compared EGYSHM SSH with satellite altimetry to verify and validate the positions and the shape of the mesoscale eddies simulated. The comparison revealed similarities in positions and shapes of mesoscale features. There was some matching between Fig. 19A and B in the western domain from 25.5–28° E, which was occupied by the Mersa-Matruh feature. The monthly RMSE averaged between models SSH and SLA from satellite was calculated. All the RMSE values were less than 0.08 m. The highest value was 0.0744 m in May, while the minimum was 0.034 m in November. These results highlight the robustness of EGYSHM SSH probably to be attributed to the better EGYSHM water flux boundary conditions with respect to MFS in 2006.

We believe the quality of the model is high enough to start operational forecasts in the Egyptian coastal zones. Future research issues will include the enlargement of the basin domain, an increase in the resolution and the definition of better Nile Delta runoff outlets. In addition, the flow of the saline water from the Suez Canal should be included in future modelling and forecasting of this area.

Acknowledgements

We are grateful to the SINCEM Lab team. Special thanks for Luca Giacomelli for his help in FORTRAN and MATLAB codes. We wish to thank the CMCC team for offering MFS products. We would like also to thank Claudia Fratianni and Marina Tonani for their constructive remarks. Special thanks to the two anonymous reviewers for helpful comments on the manuscript.

References

Adani, M., Pinardi, N., Dobricic, S., 2011. Quality assessment of a 1985–2007 Mediterranean Sea reanalysis. J. Atmos. Ocean. Technol., 569–589, http://dx.doi.org/10.1175/2010JTECHO798.1.

Alam El-Din, K.A., Sharaf El-Din, S.H., Hamza, W., 2000. Numerical simulation of the Egyptian Mediterranean Shelf circulation for better coastal management. In: Int. Conf. New Trends in Water Modeling and Environmental Engineering for Safety and Life Eco-Compatible Solutions for Aquatic Environment, Capri, Italy. July 3–7.

Beron-Vera, F.J., Ochoa, J., Ripa, P., 1999. A note on the boundary conditions for salt and freshwater balances. J. Ocean Modell. 1, 111–118.

Bignami, F., Marullo, S., Santoleri, R., 1995. Long wave radiation budget in the Mediterranean Sea. J. Geophys. Res., 2501–2514.

Blumberg, A.F., Mellor, G.L., 1987. A description of a three-dimensional coastal ocean circulation model. In: Heaps, N. (Ed.), Three Dimensional Coastal Ocean Models. American Geophysical Union, Washington, D.C (pp. 208).

Brenner, S., Murashkovsky, S., Gertman, I., 2006. Assessment of one year of high-resolution operational forecasts for the southeastern Mediterranean shelf region in the MFSTEP project. Ocean Sci. Discuss. Eur. Geosci. Union 3 (6), 2059–2085.

Budyko, M.I. (Ed.), 1963, pp. 14–26.

Buongiorno Nardelli, B., Larnicol, G., DAcunzo, E., Santoleri, R., Marullo, S., Le Traon, P.Y., 2003. Near Real Time SLA and SST products during 2-years of MFS pilot project: processing, analysis of the variability and of the coupled patterns. Ann. Geophys. 21, 103–121.

Castellari, S., Pinardi, N., Leaman, K.D., 1998. A model study of Air-Sea interaction in the Mediterranean Sea. J. Mar. Syst. 18, 89–114.

Dobricic, S., Pinardi, N., Adani, M., Tonani, M., Fratianni, C., Bonazzi, A., Fernandez, V., 2007. Daily oceanographic analyses by Mediterranean Forecasting System at the basin scale. Ocean Sci. 3, 149–157.

El-Gindy, A.A.H., Sharaf El-Din, S.H., 1985. Water masses and circulation patterns in the deep layer of the Eastern Mediterranean. In: IAMP/IAPSO Joint Assembly, August 5–16, Honolulu, Hawai, USA.

El-Gindy, A.A.H., 1984. The Study of Hydrographic and Circulation in the Eastern Mediterranean. PhD Thesis. Alexandria University, Faculty of Science, Oceanography Department.

Flather, J., 1976. A tidal model of the northwest european continental shelf. Mem. Soc. R. Sci. Liege Ser. 6 (10), 141–164.

Frihy, O.E., Debes, E.A., El Sayed, W.R., 2003. Processes resha ping the Nile delta promontories of Egypt: pre- and post -protection. Geomorphology 53, 263–279.

Garrett, C., Outerbridge, R., Thompson, K., 1993. Interannual variability in Mediterranean heat and buoyancy fluxes. J. Clim. 6, 900–910.

Gill, A.E., 1982. Atmospheric-ocean Dynamics. Acadimic Press, New York.

Halim, Y., Guergues, S.K., Saleh, H.H., 1967. Hydrographic conditions and plankton in the South East Mediterranean during the last normal Nile flood (1964). Int. Rev. Ges. Hydrobiol. 52, 401–425.

Halim, Y., 1960. Observations on the Nile bloom phytoplankton in the Mediterranean. J. Cons. Int. Explor. Mer. 26, 57–67.

Hamza, W., Ennet, P., Tamsalu, R., Zalesny, V., 2003. The 3D physical-biological model study in the Egyptian Mediterranean coastal sea. J. Aquat. Ecol. 37, 307–324.

Haney, R.L., 1991. On the pressure gradient force over steep bathymetry in sigma coordinates ocean models. J. Phys. Oceanogr. 21, 610–619.

Hecht, A., Pinardi, N., Robinson, A.R., 1988. Current water masses, eddies and Jet in the Mediterranean Levantine Basin. J. Phys. Oceangr. 18, 1320–1353.

Hellerman, S., Rosenstein, M., 1983. Normal monthly wind stress over the world ocean with error estimates. J. Phys. Oceanogr. 13, 1093–1104.

Ibrahim, O.M., 2003. A Numerical Modeling of the Circulation of the Mediterranean Egyptian Coast and Its Violation to the Levantine Basin. PhD Thesis. Oceanography Department, Alexandria University, Egypt (242 pp.).

Jerlov, N.G., 1976. Marine Optics. Elsavier Sci, New York (231 pp.).

Korres, G., Lascaratos, A., 2003. A one-way nested eddy resolving model of the Aegean and Levantine Basins: implementation and climatological runs. J. Ann. Geophys. 21, 205–220.

Korres, G., Pinardi, N., Lascaratos, A., 2000. The ocean response to low frequency interannual atmospheric variability in the Mediterranean sea. Part I. Sensitivity experiments and energy analysis. J. Clim. 13 (4), 705–731.

Legates, D.R., Willmott, C.J., 1990. Mean seasonal and spatial variability in gauge- corrected, global precipitation. Int. J. Climatol. 10, 27–111.

Ludwig, W., Dumont, E., Meybeck, M., Heussner, S., 2009. River discharges of water and nutrients to the Mediterranean and Black Sea: major drivers for ecosystem changes during past and future decades? J. Prog. Oceanogr. 80, 199–217.

Malanotte-Rizzoli, P., Manca, B.B., Ribera D'Acala, M., Theocharis, A., Bergamasco, A., Bregant, D., Budillon, G., Civitarese, G., Georgopoulos, D., Michelato, A., Sansone, E., Scarazzato, P., Souvermezoglu, E., 1997. A synthesis of the Ionian hydrography, circulation and water mass pathways during POEM—Phase I. Prog. Oceangr. 39, 153–207.

Manzella, G.M.R., Scoccimarro, E., Pinardi, N., Tonani, M., 2003. Improved near real-time data management procedures for the Mediterranean ocean Forecasting System-Voluntary Observing Ship program. Ann. Geophys. 21, 49–62.

Marchesiello, P., McWilliams, J.C., Shchepetkin, A., 2001. Open boundary conditions for long term integration of regional oceanic models. J. Ocean Modell. 3, 1–20.

Marullo, S., Buongiorno Nardelli, B., Guarracino, M., Santoleri, R., 2007. Observing the Mediterranean Sea from space: 21 years of Pathfinder-AVHRR sea surface temperatures (1985–2005): re-analysis and validation. Ocean Sci. 3, 299–310.

Mellor, G.L., Blumberg, A.F., 1985. Modeling vertical and horizontal diffusivities with sigma coordinate system. Mon. Weather Rev. 113, 1380–1383.

Mellor, G.L., Yamada, T., 1982. Development of a turbulence closure submodel for geophysical fluid problems. Rev. Geophys. Space Phys. 20, 851–875.

Mellor, G.L., Oey, L.-Y., Ezer, T., 1997. Sigma coordinate pressure gradient errors and the seamount problem. J. Atmos. Ocean. Technol. 15, 1122–1131.

Mellor, G.L., 1991. An equation of state for numerical models of ocean and estuaries. J. Atmos. Ocean. Technol. 8, 609–611.

Nittis, K., Lascaratos, A., 1998. Diagnostic and prognostic numerical studies of LIW formation. J. Mar. Syst. 18, 179–185.

Nixon, S.W., 2003. Replacing the Nile: are anthropogenic nutrients providing the fertility once brought to the Mediterranean by a great river? Ambio 32, 30–39.

Oddo, P., Pinardi, N., 2008. Lateral open boundary conditions for nested limited area models: a process selective approach. J. Ocean Modell. 20 (2), 134–156, http://dx.doi.org/10.1016/j.ocemod.2007.08.001.

POEM Group, 1992. General circulation of the Eastern Mediterranean. Earth Sci. Rev. 32, 285–309.

Pettenuzzo, D., Large, W.G., Pinardi, N., 2010. On the corrections of ERA-40 surface flux products consistentwith the Mediterranean heat and water budgets and the connection between basin surface total heat flux and NAO. J. Geophys. Res. 115, C06022, http://dx.doi.org/10.1029/2009JC005631.

Pinardi, N., Coppini, G., 2010. Operational oceanography in the Mediterranean Sea: the second stage of development. Ocean Sci. 6, 263–267.

Pinardi, N., Allen, I., Demirov, E., De Mey, P., Korres, G., Lascratos, A., Le Traon, P.Y., Maillard, C., Manzella, G., Tziavos, C., 2003. Mediterranean forecasting system: first phase of implementation (1998–2001). J. Ann. Geophys. 21, 1–21.

Pinardi, N., Arneri, E., Crise, A., Ravaioli, M., Zavatarelli, M., 2005. The physical, sedimentary and ecological structure and variability of shelf areas in the Mediterranean Sea. The Sea, vol. 4. Harvard University (chapter 32).

Pinardi, N., Zavatarelli, M., Adani, M., Coppini, G., Fratianni, C., Oddo, P., Simoncelli, S., Tonani, M., Lyubartsev, V., Dobricic, S., 2015. The Mediterranean Sea large scale low frequency ocean variability from 1987 to 2007: a retrospective analysis. Prog. Oceanogr., http://dx.doi.org/10.1016/j.pocean.2013.11.003.

Poulain, P.-M., Barbanti, R., Font, J., Cruzado, A., Millot, C., Gertman, I., Griffa, A., Molcard, A., Rupolo, V., Le Bras, S., Petit de la Villeon, L., 2007. MedArgo: a drifting profiler program in the Mediterranean Sea. Ocean Sci. 3, 379–395.

Reed, R.K., 1977. On estimating insolation over the ocean. J. Phys. Oceanogr. 17, 854–871.

Robinson, A.R., Golnaraghi, M., Lesilie, W.G., Artigiani, A., Hecht, A., Lazzoni, E., Michelato, A., Sansone, E., Theocharis, A., Unluta, U., 1991. The Eastern Mediterranean general circulation: features structure and variability. J. Dyn. Atmos. Ocean 15, 215–240.

Robinson, A.R., Malanotte-Rizzoli, P., Hecht, A., Michelato, A., Roether, W., Theocharis, A., Unluata, U., Pinardi, N., Artegiani, A., Bergamasco, A., Bishop, J., Brenner, S., Christianidis, S., Gacic, S., Georgopoulos, D., Golnaraghi, M., Hausmann, M., Junghaus, H.G., Lascaratos, A., Latif, M.A., Leslie, W.G., Lozano, C.G., Oguz, T., Ozsoy, T., Papageorgiou, E., Paschini, E., Rozentroub, Z., Sansone, E., Scarazzato, P., Schlitzer, R., Spezie, G.-C., Tziperman, E., Zodiatis, G., Athanassiadou, L., Gerges, M., Osman, M., The POEM group (Physical Oceanography of the Eastern Mediterranean), 1992. General circulation of the eastern mediterranean. J. Earth-Sci. Rev. 32, 285–309.

Rosati, A., Miyakoda, K., 1988. A general circulation model for upper ocean simulation. J. Phys. Oceanogr. 18, 1601–1626.

Roussenov, V., Stanev, E., Artale, V., Pinardi, N., 1995. A seasonal model of the Mediterranean Sea general circulation. J. Geophys. Res. 100, 13515–13538.

Said, M.A., Rajkovic, B., 1996. A study of water circulation along the Egyptian Mediterranean Coast using three dimensional numerical model. Int. J. Environ. Stud. 50, 223–235.

Said, M.A., 1990. Horizontal circulation of the Eastern Mediterranean waters during winter and summer seasons. J. Acta Adriat. 31, 1–21.

Sharaf El-Din, S.H., El-Gindy, A.A.H., 1986. Characteristics, spreading and mixing of the intermediate water mass and their seasonal variations in the Eastern Mediterranean. J. Acta Adriat. 28, 200–221.

Sharaf El-Din, S.H., Karam, A.M., 1976. Geostrophic current in the Southeastern sector of the Mediterranean Sea. J. Acta Adriat. 18, 211–235.

Smagorinsky, J., 1993. Some historical remarks on the use of nonlinear viscosities. In: Galperin, B., Orszag, S.A. (Eds.), Large Eddy Simulations of Complex Engineering and Geophysical Flows. Cambridge Univ., New York, pp. 3–36.

Sofianos, S.S., Skliris, N., Mantziafou, A., Lascaratos, A., Zodiatis, G., Lardner, R., Hayes, D., Georgiou, G., 2006. Nesting operational forecasting models in the Eastern Mediterranean: active and slave mode. Ocean Sci. Discuss. 3, 1225–1254.

Theocharis, A., Georgopoulos, D., Lascaratos, A., Nittis, K., 1993. Water masses and circulation in the central region of the Eastern Mediterranean: Eastern Ionian, South Aegean, and Northwest Levantine, 1986–1987. Deep Sea Res. Part II 40 (6), 1121–1142.

Tonani, M., Pinardi, N., Dobricic, S., Pujol, I., Fratianni, C., 2008. A high resolution free surface model on the Mediterranean sea. J. Ocean Sci. 4, 1–14.

Tonani, M., Pinardi, N., Fratianni, C., Pistoia, J., Dobricic, S., Pensieri, S., Alfonso, M., Nittis, K., 2009. Mediterranean Forecasting System: forecast and analysis assessment through skill score. Ocean Sci. 5, 649–660.

Vörösmarty, C.J., Fekete, B.M., Routheir, M., Baker, T., 1999. Global River Discharge Database, Version 1.1 (Riv.Dis.v10 supplement) (URL http://www.rivdis.sr.unh.edu).

Zodiatis, G., Lardner, R., Lascaratos, A., Georgiou, G., Korres, G., Syrmis, M., 2001. Mediterranean Forecasting System: sub-model for the Cyprus and North East Levantine Basin. Rapp. Comm. Int. Mer. Medit. 36, 90.

Zodiatis, G., Lardner, L., Hayes, D., Georgiou, G., Sofianos, S., Skliris, N., Lascaratos, A., 2006. Operational coastal ocean forecasting in the Eastern Mediterranean: implementation and evaluation. Ocean Sci. 3, 397–434.